Remote Sens. **2014**, *6*, 180-208; doi:10.3390/rs6010180

OPEN ACCESS

remote sensing

ISSN 2072-4292

www.mdpi.com/journal/remotesensing

Article

Feasibility of Ocean Acoustic Waveguide Remote Sensing (OAWRS) of Atlantic Cod with Seafloor Scattering Limitations

Ankita D. Jain [1], Anamaria Ignisca [1], Dong Hoon Yi [1], Purnima Ratilal [2] and Nicholas C. Makris [1,*]

[1] Department of Mechanical Engineering, Massachusetts Institute of Technology, Cambridge, MA 02139, USA; E-Mails: ankitadj@mit.edu (A.D.J.); anamaria.ignisca@gmail.com (A.I.); dongku@mit.edu (D.H.Y.)

[2] Department of Electrical and Computer Engineering, Northeastern University, Boston, MA 02115, USA; E-Mail: purnima@ece.neu.edu

* Author to whom correspondence should be addressed; E-Mail: makris@mit.edu; Tel.: +1-617-258-6104; Fax: +1-617-253-2350.

Received: 11 October 2013; in revised form: 4 December 2013 / Accepted: 6 December 2013 / Published: 20 December 2013

Abstract: Recently reported declines in the population of Atlantic cod have led to calls for additional survey methods for stock assessments. In combination with conventional line-transect methods that may have ambiguities in sampling fish populations, Ocean Acoustic Waveguide Remote Sensing (OAWRS) has been shown to have a potential for providing accurate stock assessments (Makris N.C., *et al*. *Science* 2009, 323, 1,734–1,737; 54th Northeast Regional Stock Assessment Workshop (54th SAW) US Department of Commerce, Northeast Fisheries Science Center, 2012). The use of OAWRS technology enables instantaneous wide-area sensing of fish aggregations over thousands of square kilometers. The ratio of the intensity of scattered returns from fish *versus* the seafloor in any resolution cell typically determines the maximum fish detection range of OAWRS, which then is a function of fish population density, scattering amplitude and depth distribution, as well as the level of seafloor scattering. With the knowledge of oceanographic parameters, such as bathymetry, sound speed structure and attenuation, we find that a Rayleigh–Born volume scattering approach can be used to efficiently and accurately estimate seafloor scattering over wide areas. From hundreds of OAWRS measurements of seafloor scattering, we determine the Rayleigh–Born scattering amplitude of the seafloor, which we find has a $f^{2.4}$ frequency dependence below roughly 2 kHz in typical continental shelf environments along the US northeast coast. We then find that it is possible to robustly detect cod

aggregations across frequencies at and near swim bladder resonance for observed spawning configurations along the U.S. northeast coast, roughly the two octave range 150–600 Hz for water depths up to roughly 100 m. This frequency range is also optimal for long-range ocean acoustic waveguide propagation, because it enables multimodal acoustic waveguide propagation with minimal acoustic absorption and forward scattering losses. As the sensing frequency moves away from the resonance peak, OAWRS detection of cod becomes increasingly less optimal, due to a rapid decrease in cod scattering amplitude. In other environments where cod depth may be greater, the optimal frequencies for cod detection are expected to increase with swim bladder resonance frequency.

Keywords: acoustic remote sensing; wide-area fish detection; OAWRS; waveguide propagation; Atlantic cod; fisheries; seafloor scattering

1. Introduction

Reported declines [1–5] in the population of Atlantic cod have led to calls for additional survey methods for stock assessments, specifically the use of Ocean Acoustic Waveguide Remote Sensing (OAWRS) in the Gulf of Maine [6–8]. Recently, OAWRS techniques have been shown to be capable of instantaneous wide-area sensing of marine life over thousands of square kilometers [9,10]. Dwindling cod populations have a potential to affect long-term ecological balance [11–13] and the sustainability of the cod fishery along the US northeast coast [14]. Cod assessments typically incorporate data collected from conventional acoustic and trawl line transect surveys [15–19] that may lead to ambiguities in population estimates [17,20,21]. The combination of conventional methods and OAWRS techniques, however, has a potential for accurately estimating fish stocks over ecosystem-scale areas [9,22]. Here, we assess the feasibility of OAWRS detection and enumeration of cod in typical continental shelf waveguide environments along the US northeast coast. We do so by combining ocean-acoustic waveguide propagation modeling [9,10] that has been calibrated in a variety of continental shelf environments for OAWRS applications with a model for cod scattering that matches well with measured data [23] for cod scattering.

Both OAWRS detection range and minimum detectable fish population density are limited by scattered returns from the seafloor in the same resolution cell as the fish. Efficient and reliable estimates of seafloor scattering are then necessary to determine OAWRS fish detection limitations. Here, we use a Rayleigh–Born volume scattering approach, where multimodal propagation effects, which appear only in the waveguide Green function, can be mathematically separated from seafloor scattering effects. Our approach differs from traditional investigations of seafloor scattering using free-space plane-wave approaches [18,24], which often do not efficiently or effectively translate to multimodal propagation and scattering in an acoustic waveguide [25–27]. We estimate seafloor scattered returns by applying the Rayleigh–Born approximation to Green's theorem [28]. From hundreds of measurements of seafloor scattering in continental shelf waveguide environments along the US northeast coast, we determine

key statistics of the Rayleigh–Born seafloor scattering amplitude for various source frequencies. We show that OAWRS techniques are capable of robustly detecting Atlantic cod above seafloor scattering at and near their swim bladder resonance frequencies. These frequencies also happen to be optimal for long-range propagation in an ocean waveguide. Away from the swim bladder resonance frequencies, OAWRS detection of cod can become less optimal, due to rapid decreases in the cod scattering amplitude.

2. Data Collection

2.1. Seafloor Scattering Data Collection during OAWRS Experiments

We used OAWRS seafloor scattering data acquired in 2003 on the New Jersey continental shelf [10,29] and in 2006 on the northern flank of Georges Bank in the Gulf of Maine [9,30] (Figure A.1). The areas investigated for study here had relatively constant bathymetry with sandy bottoms of mean density and sound speed, 1.9 g/cm^3 and 1700 m/s, respectively [27,30,31]. Hundreds of sound speed profile samples of the water column were taken during the experiments to allow accurate characterization of both the mean and randomly fluctuating components of the continental shelf waveguide. Here, by "scattered returns" we mean the OAWRS source signal that is scattered from a target, such as fish or seafloor, and received at the OAWRS horizontal receiver array, typically measured in decibel units (dB re 1 μPa).

Figure 1. Echograms showing cod aggregations on (**A**,**B**) 28–29 May and (**C**,**D**) 18–19 June 2011, off the coasts of Massachusetts and New Hampshire in Ipswich Bay during the same University of New Hampshire surveys described in [32,33]. The color bar shows the volume density in the number of cod/m^3. Black regions represent seafloor sediment.

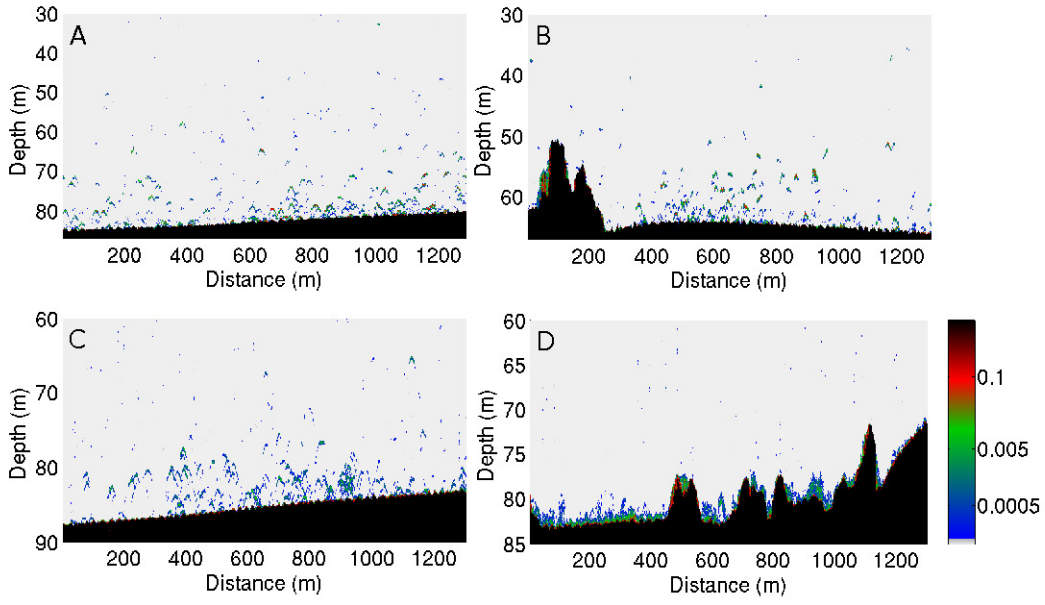

2.2. Measured Distribution of Atlantic Cod in Massachusetts State Waters

We used cod body length distributions and aggregation densities measured during recent spring surveys conducted from New Hampshire during May–June, 2011, described in [32,33]. The surveys

were conducted just south of the Isle of the Shoals and entered the Gulf of Maine Cod Spawning Protection Area just a few nautical miles east of the northern Massachusetts coastline [34]. A scientific echo sounder with a 120-kHz split beam transducer produced range-depth images of cod aggregations [32,33], as shown in Figure 1. Spawning aggregations imaged along the survey tracks were found to have areal population densities of roughly 0.01 cod/m^2 [32,33]. Concurrent trawls found a mean cod length of roughly 66 cm (Figure 2) [32,33]. The most dense cod aggregations were found within roughly 10 m of the seafloor, where the water depth varied between roughly 50 to 90 m (Figure 1) [32,33]. These recent measurements of cod during spawning are used to provide examples of cod distributions, from which the feasibility of using OAWRS to detect cod aggregations is assessed. Since no cod were found in trawls during the Northeast Fisheries Science Center Georges Bank Atlantic Herring survey [35] that was conducted in conjunction with an OAWRS survey during the peak fall herring spawning in 2006, no ground truth experimental comparisons between OAWRS detections and known cod aggregations are available.

Figure 2. (**A**) The distribution of cod body length derived from Gurshin *et al.* [32]. The estimated target strength of a cod at different depths following the body-length distribution in (A) measured during Ipswich Bay spring surveys conducted in May–June, 2011 [32,33], for neutral buoyancy depths (**B**) at 70 m, (**C**) near the sea-surface and (**D**) at 300 m. Large variations in body lengths of cod during surveys are common and lead to variations in swim bladder resonance frequency and peak target strength for different fish depths in the water column. All depths are measured from the sea-surface. The target strength of cod is estimated using the Love model [36].

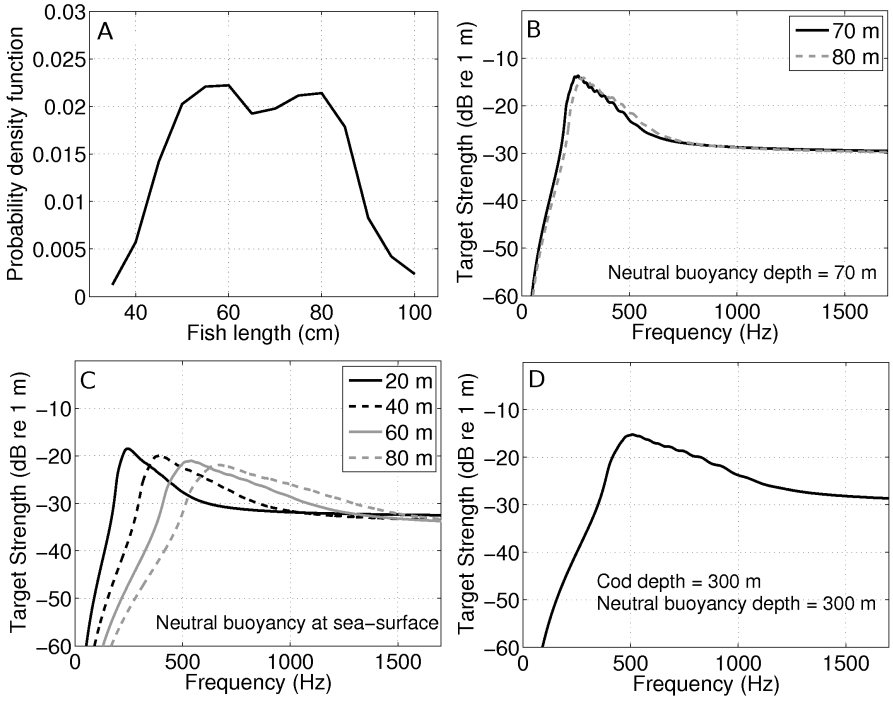

3. Methods

3.1. Estimation of Rayleigh–Born Seafloor Scattering Amplitude Statistics from Measured Seafloor Scattering

The expected magnitude squared of the Rayleigh–Born seafloor scattering amplitude, $\langle|\mathrm{A}_S|^2\rangle$, is estimated by minimizing the mean squared error between the measured and modeled scattered field (Equation (11)) over range with respect to $\widehat{|\mathrm{A}_S|^2}$. For the m^{th} radial beam of the j^{th} transmission, an estimate, $\widehat{|\mathrm{A}_S|^2}^j_m$, is obtained by minimizing the sum of the mean squared error over L OAWRS range resolution cells, so that:

$$[\widehat{|\mathrm{A}_S(f_c)|^2}^j_m] = \min_{|\mathrm{A}_S|^2} \frac{1}{L}\sum_{i=1}^{L}\left|10\log(\frac{|\Phi^j_{m^{Data}}(\mathbf{r}_{S_i}|\mathbf{r},\mathbf{r}_0,f_c)|^2}{\mathbb{P}^2_{ref}}) - 10\log(\frac{\mathrm{Var}(\Phi_m(\mathbf{r}_{S_i}|\mathbf{r},\mathbf{r}_0,f_c))}{\mathbb{P}^2_{ref}})\right|^2 \quad (1)$$

where $|\Phi^i_{m^{Data}}(\mathbf{r}_{S_i}|\mathbf{r},\mathbf{r}_0,f_c)|^2$ is the measured scattered field and $\mathrm{Var}(\Phi_m(\mathbf{r}_{S_i}|\mathbf{r},\mathbf{r}_0,f_c))$ is the variance of the modeled scattered field; a good approximation to the second moment of the scattered field (Equations (A.17) and (A.18)), at the i^{th} OAWRS range resolution cell centered on $\mathbf{r}_{S_i}$ and $\mathbb{P}_{ref}$, is 1 μPa/Hz in water. The estimate of $\langle|\mathrm{A}_S(f_c)|^2\rangle$ for each source frequency, f_c, is then the mean of $\widehat{|\mathrm{A}_S(f_c)|^2}^j_m$ over M radial beams and J transmissions:

$$\langle\widehat{|\mathrm{A}_S(f_c)|^2}\rangle = \frac{\sum_{j=1}^{J}\sum_{m=1}^{M}\widehat{|\mathrm{A}_S(f_c)|^2}^j_m}{JM} \quad (2)$$

We restrict our analysis to beams that are not contaminated by bio-clutter or ship noise and to regions that are within approximately 30 km of the receiver array (Figure A.1). We have excluded the beams where the scattered returns from the seafloor fall below the local ambient noise in the same beam. Seafloor scattered returns can be distinguished from fish scattered returns in OAWRS images, because (i) they have different frequency dependence from fish scattered returns [9,10,30] and (ii) they are statistically stationary in time as opposed to non-stationary returns from fish aggregations [9,10,27,30,37].

Comparisons between the measured and modeled scattered field level in the New Jersey continental shelf and Georges Bank for various source frequencies are shown in Figures A.2 and A.3, respectively. We find that the mean modeled seafloor scattered level matches well (within one standard deviation) with the respective mean measured scattered level over a given resolution cell along the entire sensing range for most frequencies that have been used for OAWRS sensing in the past. The 1,325-Hz New Jersey continental shelf scattered field data (Figure A.2C) may be contaminated by diffusely distributed scatterers in the water column that affect the range-dependence of the scattered field.

3.2. Fish-to-Seafloor Scattering Ratio

For a given fish aggregation density of N fish in the water column per unit area, the second moment of total scattered field from all N fish [10,38] is:

$$\left\langle|\Phi_F(N)|^2\right\rangle = N\left\langle|\Phi_F(1)|^2\right\rangle \quad (3)$$

where $\Phi_F(1)$ is the scattered field from one fish per unit area. For the fish aggregation to be detectable, the expected magnitude squared of the scattered field from N fish, $\langle|\Phi_F(N)|^2\rangle$, should be greater than that from the seafloor, $\langle|\Phi_S|^2\rangle$, over the same area:

$$N\left\langle|\Phi_F(1)|^2\right\rangle > \left\langle|\Phi_S|^2\right\rangle \tag{4}$$

or:

$$\text{FSR} = \frac{N\left\langle|\Phi_F(1)|^2\right\rangle}{\left\langle|\Phi_S|^2\right\rangle} > 1 \tag{5}$$

where FSR is the fish-to-seafloor scattering ratio. Then, the minimum required number of fish per unit area, N_{min}, above which fish scattering is greater than seafloor scattering is:

$$N_{\text{min}} = \frac{\langle|\Phi_S|^2\rangle}{\langle|\Phi_F(1)|^2\rangle} \tag{6}$$

As a direct consequence of Equation (5), FSR decreases with decreasing fish aggregation density, and so, it becomes harder to detect less dense fish aggregations above seafloor scattering within a given OAWRS resolution footprint.

4. Results

4.1. Experimental Estimation of Rayleigh-Born Seafloor Scattering Amplitude

Using OAWRS measurements of long-range seafloor scattering in typical sandy continental shelf waveguide environments along the US northeast coast, we estimate the magnitude squared of seafloor scattering amplitude per coherence volume (Figure 3) over the range of frequencies that are conducive for long-range waveguide propagation and where the scattering amplitude of fish aggregations is high due to swim bladder resonance. We find that seafloor scattering amplitude squared follows a roughly $f^{2.4}$ frequency dependence, varying as $f^{2.7}$ in the New Jersey continental shelf and as $f^{2.1}$ in Georges Bank (Figure 3). At all source frequencies, the magnitudes of seafloor scattering amplitudes in the two continental shelf environments match well with each other (Figure 3), consistent with the similarity in sandy sediments found in these two regions [9,10]. Seafloor scattering is modeled using a Rayleigh–Born approach in terms of the incoming Green function from an acoustic source to a seafloor scattering volume element, the Rayleigh–Born seafloor scattering amplitude and an outgoing Green function from the seafloor scattering volume element to a receiver, integrated over the entire scattering volume in the seafloor (Section 4.3). Multimodal propagation effects appearing in waveguide Green functions [28,39] can be mathematically separated from seafloor scattering effects. In order to account for random fluctuations in the ocean waveguide, the moments of Green functions and their derivatives are calculated by Monte Carlo realizations over range- and depth-dependent sound speed structures [29,30,37].

Figure 3. Frequency dependence of the experimentally estimated magnitude squared of seafloor scattering amplitude, $|A_S|^2$ (Equation (12)), which is proportional to the scattering cross-section, in terms of a volume adjusted target strength defined as $\mathrm{TS}_S = 10\log_{10}\left(\frac{|A_S|^2}{V_{ref}/r_{ref}^4}\right)$, for the New Jersey continental shelf (gray circles) and Georges Bank environment (black circles) along with the respective standard deviations (solid tick marks). The overall frequency dependence of the magnitude squared of seafloor scattering amplitude per coherence volume for both environments is approximately $f^{2.4}$. In water, V_{ref} = 1 m^3 and r_{ref} = 1 m.

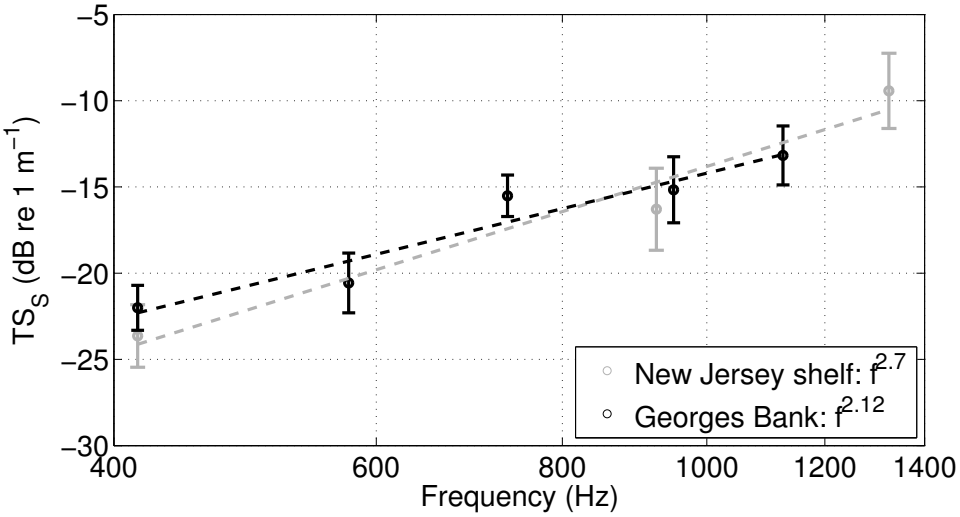

4.2. OAWRS Detection of Atlantic Cod Aggregations and Individuals

We find that at swim bladder resonance frequencies, robust detection and imaging of cod spawning aggregations with OAWRS is possible (Figures 1 and 2) in continental shelf waveguide environments along the US northeast coast. Our analysis shows that scattered returns from bottom-dwelling spawning cod aggregations, which were observed by echosounders during recent spring surveys in Ipswich Bay [32,33], with population densities of 0.01 fish/m^2, can be detected roughly 20–27 dB above seafloor scattered returns at swim bladder resonance, roughly 300 Hz in this case, when cod are neutrally buoyant close to the seafloor (Figure 4A,B). This spawning cod aggregation density is roughly 2–3 orders of magnitude larger than the minimum density necessary for OAWRS detection above seafloor scattering for ranges up to and beyond 30 km, as shown in Figure 4B. Similarly robust OAWRS detection is possible for cod spawning aggregations during mid-water column feeding [40,41] up to 30 km and beyond, when probed at a swim bladder resonance frequency of roughly 200 Hz, for cod neutrally buoyant in the mid-water column (Figure 4C,D). Individually dispersed cod located in the mid-water column can also be robustly detected within a few kilometers using OAWRS when probed at the swim bladder resonance frequency (Figure 5). In the extreme case of cod being neutrally buoyant at the sea surface and, so, at their negative buoyancy limit anywhere in the water column [42–45], the swim bladder resonance frequency will increase and the cod scattering amplitude will decrease (Figure 2C), so that the fish-to-seafloor scattering ratio (FSR) (Equation (5)) will decrease by roughly 8 dB for the bottom dwelling case of Figure 4A,B and by roughly 5 dB for the mid-water column case of Figure 4C,D.

Figure 4. The Ocean Acoustic Waveguide Remote Sensing (OAWRS) fish-to-seafloor scattering ratio (FSR) (Equation (5)) as a function of frequency and the normalized scattered returns from cod *vs.* seafloor for various cod configurations in the water column of a depth of 80 m. The minimum population density required for OAWRS detection of cod at or near the swim bladder resonance is roughly 1×10^{-4} cod/m^2 for bottom-dwelling cod and roughly 1×10^{-5} cod/m^2 for mid-water column cod. Cod are assumed to be neutrally buoyant at the shallowest limit of their assumed occupancy depth range in each case. The aggregation density in (**A**)–(**B**) is 0.01 cod/m^2, similar to that observed during spawning in Ipswich Bay [32,33], and in (**C**)–(**D**) is 0.001 cod/m^2, similar to that observed during feeding [40,41]. The cod body length is assumed to follow the distribution measured during a recent Ipswich Bay spring survey in 2011, as shown in Figure 2. Methods for the estimation of FSR and the scattered returns are described in Sections 3.2 and 4.3.

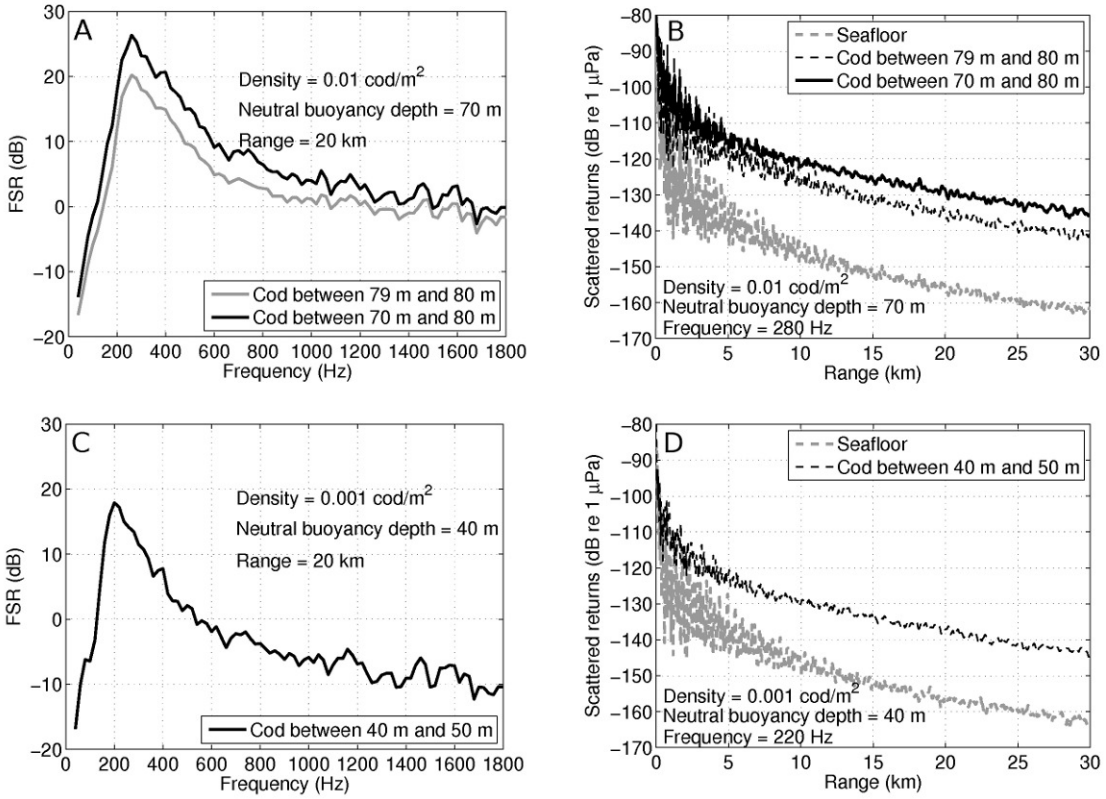

The spawning aggregation density then would be roughly 1–2 orders of magnitude higher than the minimum density required for OAWRS detection above seafloor scattering, again enabling robust OAWRS detection. At spawning sites with denser cod aggregations [46], the FSR is expected to be higher, and so, the cod will be robustly detectable over a wider range of frequencies near swim bladder resonance. In the case of cod found in deeper Gulf of Maine waters located and neutrally buoyant close to the seafloor [47], the swim bladder resonance frequency increases and cod scattering amplitude decreases (Figure 2D), so that the fish-to-seafloor scattering ratio (FSR) (Equation (5)) decreases. For example, this decrease is roughly 5–6 dB from that shown in Figure 4A for cod at 300 m of depth with a population density of 0.01 fish/m^2. This aggregation density then would be roughly 1–2 orders of magnitude higher than the minimum density required for OAWRS detection above seafloor scattering, again enabling

robust OAWRS detection. The scattering amplitude of Atlantic cod is modeled as a function of frequency using the Love model [36] for a given body length distribution and an occupancy depth in the water column. Our theoretical predictions of cod swim bladder resonance from the Love model [36] match well with past swim bladder resonance measurements of cod [23] made at similar depths. The scattered field from cod are modeled using this scattering amplitude and the waveguide Green function determined by parabolic equation calculations given known water column and sediment sound speed structures and bathymetry and using the methods described in Appendix C of Jagannathan *et al.* [37]. Cod densities are assumed to be uniform within the resolution footprint of the OAWRS system. This is easily attained for OAWRS range resolution $\Delta r = c/(2B)$, which is typically on the order of 15 m and set by the signal bandwidth, B [10]. It is also typically attained in cross-range $\Delta S = R(\lambda/L)$ out to ranges of at least 30 km, where ΔS typically is less than the roughly 1 km extent of spawning cod aggregations (Figure 1) [32,48] for typical 128-element receiver arrays sampled at half-wavelength spacing [9,10]. The seafloor scattering amplitude in the Ipswich Bay environment considered here is expected to be similar to that estimated in the New Jersey continental shelf and Georges Bank environments (Section 4.1, Figure 3), due to similar [49] sediment types.

Figure 5. The fish-to-seafloor scattering ratio (FSR) (Equation (5)) as a function of range for OAWRS detection of a single cod at the swim bladder resonance frequency. An individual cod can be detected at least 10 dB above the seafloor scattering when suspended at mid-water column within roughly 8 km of the source, but may not be detected when located on or very close to the seafloor when probed at the swim bladder resonance frequency. The cod is assumed to be neutrally buoyant at its occupancy depth in the water column. The cod is assumed to have a body-length distribution shown in Figure 2A. The seafloor is assumed to have a uniform depth of 80 m. The source and receiver are located at 50 m of depth. Methods for estimation of FSR are described in Section 3.2.

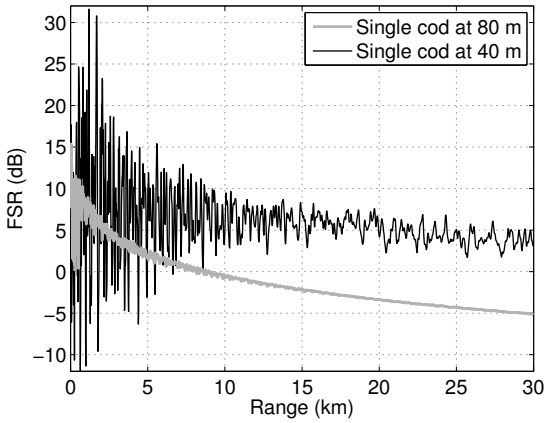

Spawning cod aggregations in the coastal waters under investigation here have recently been shown to produce sounds in the 50–500 Hz frequency range [50,51]. The fact that these cod sounds are in the *same* frequency range as our theoretical predictions of swim bladder resonance for spawning cod aggregations is expected, because the cod sound production mechanism involves stimulation of the swim bladder [52,53], which produces the largest response at resonance. These cod sounds would not affect active OAWRS cod sensing, because their levels are well below active OAWRS scattered returns

and are also incoherent with respect to OAWRS scattered returns, which reduces their effect as noise even further by the coherent matched filtering used in OAWRS detection and imaging [9,10].

4.3. Theoretical Derivation of Rayleigh–Born Seafloor Scattering Amplitude

The seafloor scattered field at center frequency, f_c, can be written from Equation (A.5) as:

$$\Phi_S(\mathbf{r}_S|\mathbf{r},\mathbf{r}_0,f_c) = (4\pi)\iiint_{V_S}[k^2\Gamma_\kappa(\mathbf{r}_t)G(\mathbf{r}_t|\mathbf{r}_0,f_c)G(\mathbf{r}|\mathbf{r}_t,f_c) + \Gamma_d(\mathbf{r}_t)\nabla G(\mathbf{r}_t|\mathbf{r}_0,f_c)\cdot\nabla G(\mathbf{r}|\mathbf{r}_t,f_c)]dV_t \quad (7)$$

where $\Phi_S(\mathbf{r}_S|\mathbf{r},\mathbf{r}_0,f_c)$ is the seafloor scattered field for an OAWRS source located at $\mathbf{r}_0$, a scattering seafloor region centered on $\mathbf{r}_S$ and an OAWRS receiver located at $\mathbf{r}$; Γ_k is the fractional change in seafloor compressibility; Γ_d is the fractional change in seafloor density; V_S is the volume of the scattering seafloor patch determined by the resolution footprint of the sensing system; $k = 2\pi f_c/c$ is the acoustic wavenumber; c is the sound speed; $G(\mathbf{r}_t|\mathbf{r}_0,f_c)$ is the Green function from the source to the elemental patch centered on $\mathbf{r}_t$ within V_S; and $G(\mathbf{r}|\mathbf{r}_t,f_c)$ is the Green function from the patch to the receiver.

Since the mean scattered field from diffuse inhomogeneities in a fluctuating waveguide vanishes [54–57], the second moment of the seafloor scattered field is well approximated by its variance (Equations (A.17) and (A.18)):

$$\begin{aligned}\mathrm{Var}(\Phi_S(\mathbf{r}_S|\mathbf{r},\mathbf{r}_0,f_c)) &= (4\pi)^2\iiint_{V_S}V_c(\mathbf{r}_S,z_t)k^4\mathrm{Var}(\Gamma_\kappa)\langle|G(\mathbf{r}_t|\mathbf{r}_0,f_c)|^2|G(\mathbf{r}|\mathbf{r}_t,f_c)|^2\rangle dV_t,\\ &+ (4\pi)^2\iiint_{V_S}V_c(\mathbf{r}_S,z_t)\mathrm{Var}(\Gamma_d)\langle|\nabla G(\mathbf{r}_t|\mathbf{r}_0,f_c)\cdot\nabla G(\mathbf{r}|\mathbf{r}_t,f_c)|^2\rangle dV_t,\\ &+ (4\pi)^2\iiint_{V_S}V_c(\mathbf{r}_S,z_t)k^2\mathrm{Covar}(\Gamma_\kappa,\Gamma_d)\\ &\langle 2\Re\{G(\mathbf{r}_t|\mathbf{r}_0,f)G(\mathbf{r}|\mathbf{r}_t,f_c)\nabla G^*(\mathbf{r}_t|\mathbf{r}_0,f_c)\cdot\nabla G^*(\mathbf{r}|\mathbf{r}_t,f_c)\}\rangle]\,dV_t \quad (8)\end{aligned}$$

where V_c is the coherence volume of inhomogeneities and $\Re\{.\}$ represents the real part. Here: (i) the integral term with waveguide Green functions sums monopole scattering contributions; (ii) the integral term with the gradients of waveguide Green functions sums dipole scattering contributions; and (iii) the integral term with Green functions and their gradients contains cross terms. Since the integrals (ii) and (iii) are found to be proportional to the integral (i) in Section A.2, we define proportionality constants F_d and F_c, such that:

$$\begin{aligned}&\mathrm{Var}(\Phi_S(\mathbf{r}_S|\mathbf{r},\mathbf{r}_0,f_c)) \quad (9)\\ &= \iiint_{V_S}k^4V_c[\mathrm{Var}(\Gamma_k) + F_d\mathrm{Var}(\Gamma_d) + F_c\mathrm{Cov}(\Gamma_k,\Gamma_d)]\\ &\quad (4\pi)^2\langle|G(\mathbf{r}_t|\mathbf{r}_0,f_c)|^2|G(\mathbf{r}|\mathbf{r}_t,f_c)|^2\rangle dV_t\end{aligned}$$

The variance of the seafloor scattered field can also be written as:

$$\begin{aligned}&\mathrm{Var}(\Phi_S(\mathbf{r}_S|\mathbf{r},\mathbf{r}_0,f_c)) \quad (10)\\ &= \iiint_{V_S}\frac{(4\pi)^2}{V_c}\left\langle\left|\frac{S(f_c,\mathbf{r}_t)}{k}\right|^2\right\rangle\langle|G(\mathbf{r}_t|\mathbf{r}_0,f)|^2|G(\mathbf{r}|\mathbf{r}_t,f)|^2\rangle dV_t\end{aligned}$$

where $S(f, \mathbf{r}_t)$ is the scatter function of seafloor inhomogeneities contained within a single coherence volume centered on $\mathbf{r}_t$ (Section A.3). Then, for relatively constant moments of fractional changes in seafloor density and compressibility across OAWRS spatial scales, we can write Equation (9) as:

$$\begin{aligned} &\mathrm{Var}(\Phi_S(\mathbf{r}_S|\mathbf{r}, \mathbf{r}_0, f_c)) \\ &\quad = \left\langle |\mathrm{A}_S(f_c, \Gamma_k, \Gamma_d, V_c)|^2 \right\rangle \iiint_{V_S} (4\pi)^2 \langle |G(\mathbf{r}_t|\mathbf{r}_0, f_c)|^2 |G(\mathbf{r}|\mathbf{r}_t, f_c)|^2 \rangle dV_t \end{aligned} \tag{11}$$

where the expected magnitude squared of the seafloor scattering amplitude per coherence volume is defined as:

$$\begin{aligned} \left\langle |\mathrm{A}_S(f_c, \Gamma_k, \Gamma_d, V_c)|^2 \right\rangle &= \frac{1}{V_c} \left\langle \left| \frac{S(f_c)}{k} \right|^2 \right\rangle \\ &= k^4 V_c [\mathrm{Var}(\Gamma_k) + F_d \mathrm{Var}(\Gamma_d) + F_c \mathrm{Cov}(\Gamma_k, \Gamma_d)] \end{aligned} \tag{12}$$

which is a function of insonification frequency and seafloor properties, such as changes in seafloor density, compressibility and coherence length scale.

Detailed derivations of the broadband seafloor scattered field and its moments and approximations that enable efficient wide-area estimation of seafloor scattering using the Rayleigh–Born approach are provided in Appendices A.1–A.4.

5. Discussion

A lower frequency OAWRS system [9,10] spanning the cod swim bladder resonance frequencies may be used to continuously detect, monitor and enumerate cod populations and to quantitatively describe their temporal and spatial behavior. Widely separated population centers (Figure 6A) can be identified by the continuous spatial coverage of OAWRS imaging, but may be missed by conventional acoustic and trawl line transect approaches. A typical scenario for wide-area sensing using OAWRS is given in Figure 6, where almost the entire Massachusetts and New Hampshire coastal region, including the Gulf of Maine Cod Spawning Protection Area [34], can be surveyed in 75 s within the corresponding 100-km diameter OAWRS imaging window. The OAWRS coverage area in Figure 6B includes some of the prime spawning locations of Atlantic cod in the Gulf of Maine, where they are known to form dense aggregations [47,58] that should be robustly detectable using OAWRS techniques. The OAWRS approach typically employs a towed receiver array that moves along tracks and, so, produces hundreds of instantaneous overlapping imaging windows [9,10]; some of these are shown in Figure 6B, where the centers of the circles correspond to the location of the tow ship when the image was formed. Since detection ranges in OAWRS typically span many tens to hundreds of water column depths, ocean depth is very shallow compared to the OAWRS sensing range in continental shelf environments [9,10] and enables hundreds to thousands of propagating acoustic modes to fill the entire water column at OAWRS frequencies [24,59–61]. Only at potential nulls within an eighth of the acoustic wavelength from potential pressure release surfaces at the water column's upper and lower boundaries may fish detection become difficult to effectively impossible, as in any acoustic sensing system. Consistent application of National Oceanic and Atmospheric Administration (NOAA) guidelines on sound in the ocean [62] suggests that many ships with continuous engine noise, such as cruise ships, cargo

vessels and whale-watching boats [63–65], should monitor for marine mammals within a few to tens of kilometers of the ship, but that OAWRS, which uses short, infrequent pulses of low duty cycle (roughly 0.01) and whose received sound pressure levels never exceed those of natural marine mammal vocalizations [66–68], should monitor for marine mammals within tens to hundreds of meters from the OAWRS source.

Figure 6. (**A**) Distribution of cod spawning populations during the Industry-Based Survey for Gulf of Maine Cod conducted by the Massachusetts Division of Marine Fisheries in 2006 [69] with the typical OAWRS areal coverage of 100 km in 75 s and 50 km in 35 s. (**B**) Bathymetry of the region off the coast of Massachusetts and the typical OAWRS areal coverage of 100 km in 75 s and 50 km in 35 s. The Gulf of Maine cod spawning protection area [34] and May–June, 2011, University of New Hampshire Cod Survey area [32,33] falls in the Ipswich Bay, off the coast of Massachusetts and New Hampshire. A towed receiver array typically employed in OAWRS moves along tracks that would run between the centers of the shown circles and produce effectively continuous overlapping imaging windows in between.

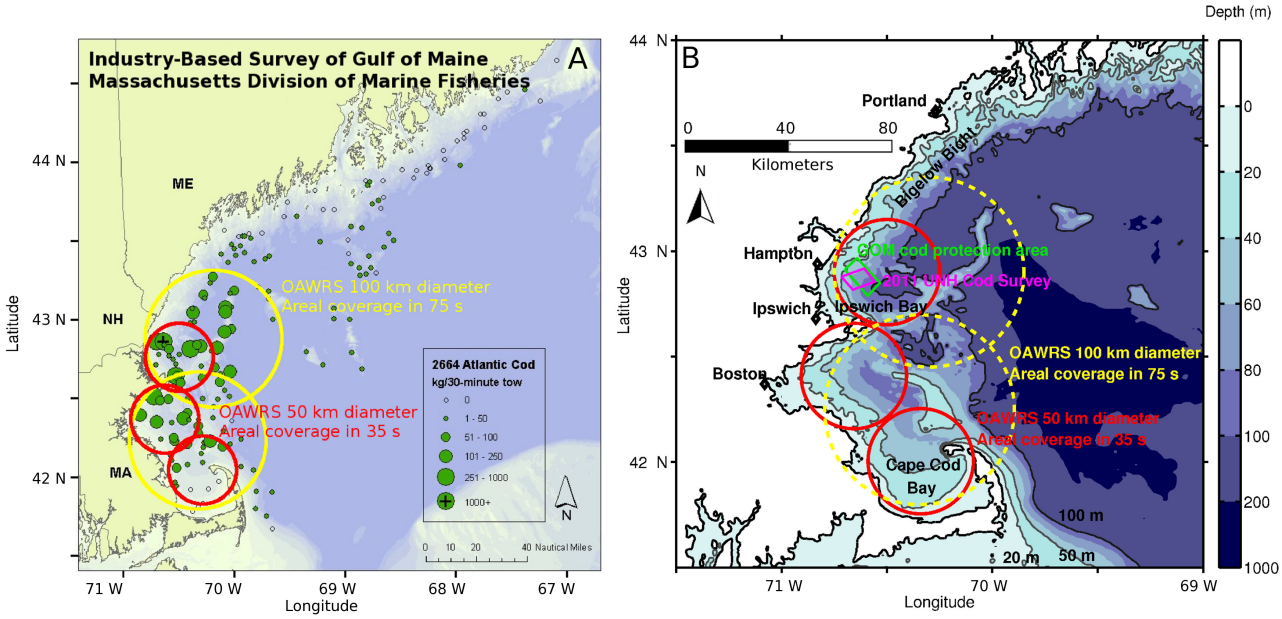

It may be possible to remotely classify cod by OAWRS spectral analysis, since they have such a strong response at their swim bladder resonance, which is not found in seafloor scattering. Ground truth from capture, as well as behavioral analysis to set the context would still likely be necessary, since a number of other species of large fish, such as haddock, hake and pollock [70], may have resonant responses in similar frequency ranges (Figure 7). It should, however, be possible to remotely distinguish cod from smaller groundfish species that have resonance responses at frequencies hundreds of Hertz greater than those of cod, as shown in Figure 7 for plaice and redfish. Cod surveys are typically conducted during the spawning season, when cod aggregations are largest and densest [34,58], making concurrent ground truth verification possible by capture trawl. During off-spawning seasons, however, capture trawl may not be practical for the typical widely dispersed cod populations, so increasing the need for classification by remote techniques, such as OAWRS spectral analysis.

Figure 7. (**A**) The distribution of body lengths of some other groundfish species found along the coasts of Massachusetts and New Hampshire during spring 2005–2006 [69,71]. (**B**) The estimated target strength of these fish species following the body-length distribution in (A), located between 70 m and 80 m in the water column and neutrally buoyant at 70 m. All depths are measured from the sea-surface. The target strength of the different species is estimated using the Love model [36].

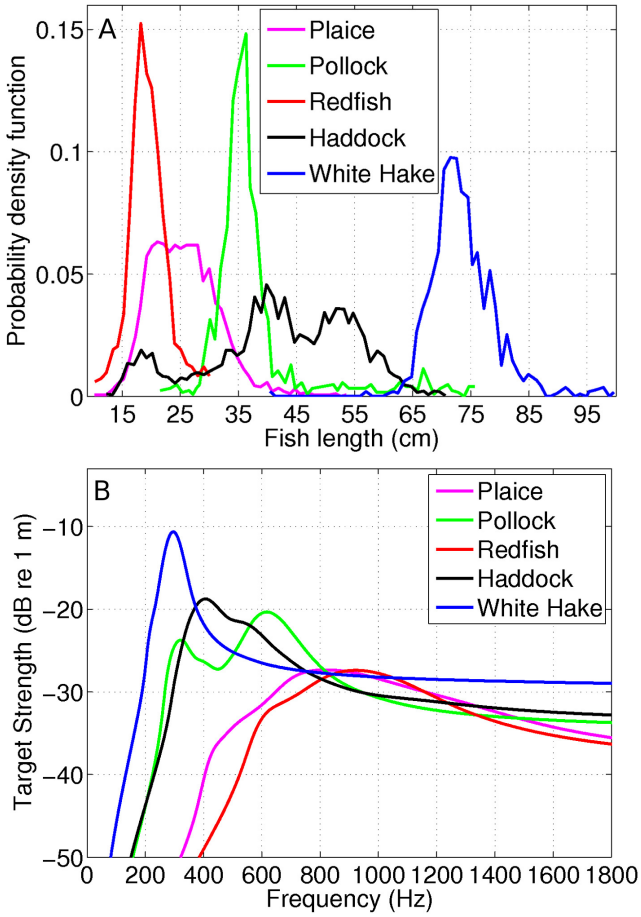

6. Conclusions

We find that Ocean Acoustic Waveguide Remote Sensing (OAWRS) is capable of instantaneously and robustly detecting spawning cod aggregations over wide areas spanning thousands of square kilometers for observed spawning cod densities and configurations in US northeast continental shelf waters at cod swim bladder resonance frequencies. At swim bladder resonance, OAWRS can also be used to detect individual cod within a few kilometers of the OAWRS system. Such robust detections of cod are possible, because the cod scattering amplitude has a strong low frequency resonance peak spanning the roughly two-octave range of 150–600 Hz within water depths of roughly 100 m, in contrast to the relatively uniform seafloor scattering frequency dependence of roughly $f^{2.4}$, which we find below roughly 2 kHz in US northeast continental shelf environments. This cod resonance frequency range is also optimal for long-range ocean acoustic waveguide propagation, because it enables multimodal acoustic waveguide propagation with minimal acoustic absorption and forward scattering losses. As the sensing frequency moves away from the resonance peak, OAWRS detection of cod becomes increasingly

less optimal, due to a rapid decrease in cod scattering amplitude. In other environments where cod depth may be greater, the optimal frequencies for cod detection are expected to increase with swim bladder resonance frequency.

Acknowledgments

This research was supported by the National Oceanographic Partnership Program, the Office of Naval Research and the National Oceanic and Atmospheric Administration (NOAA). We would like to thank Christopher W. D. Gurshin, W. Huntting Howell and J. Michael Jech for inviting us to take part in the cod surveys conducted in Ipswich Bay in May–June, 2011, and for providing us with raw echogram data.

Conflicts of Interest

The authors declare no conflict of interest.

References

1. Northeast Fisheries Science Center. *Ecology of the Northeast US Continental Shelf—Human Dimension*; Technical Report; NFSC, National Oceanic And Atmospheric Administration: Woods Hole, MA, USA, 2012.
2. Northeast Regional Office. *2011 Gulf of Maine Cod Baseline Assessment*; Technical Report; Northeast Regional Office, National Oceanic And Atmospheric Administration: Gloucester, MA, USA, 2012.
3. Northeast Fisheries Science Center. *55th Northeast Regional Stock Assessment Workshop (55th SAW): Assessment Summary Report*; Ref Doc. 13-01; National Marine Fisheries Service: Woods Hole, MA, USA, 2013; p. 41.
4. Myers, R.; Hutchings, J.; Barrowman, N. Hypotheses for the decline of cod in the North Atlantic. *Mar. Ecol. Progr. Series* **1996**, *138*, 293–308.
5. Hutchings, J. Spatial and temporal variation in the density of northern cod and a review of hypotheses for the stock's collapse. *Can. J. Fish. Aquat. Sci.* **1996**, *53*, 943–962.
6. Kerry, J. *Following Field Hearing, Kerry Presses Urgent Next Steps to Aid Fishermen*; Press Release: Washington, D.C., USA, 2011.
7. Kerry, J. *Kerry Urges New Cod Assessment, Preparations for Economic Relief*; Press Release: Washington, D.C., USA, 2011.
8. *Hearing Before the Subcommittee on Oceans, Atmosphere, Fisheries, and Coast Guard, One Hundred Twelfth Congress, First Session US Senate Committe on Commerce, Science, and Transportation, March 8 2011*; Technical Report; United States Senate, Govt. of United States: Washington, DC, USA, 2011.
9. Makris, N.C.; Ratilal, P.; Jagannathan, S.; Gong, Z.; Andrews, M.; Bertsatos, I.; Godo, O.R.; Nero, R.W.; Jech, J.M. Critical population density triggers rapid formation of vast oceanic fish shoals. *Science* **2009**, *323*, 1734–1737.
10. Makris, N.C.; Ratilal, P.; Symonds, D.T.; Jagannathan, S.; Lee, S.; Nero, R.W. Fish population and behavior revealed by instantaneous continental shelf-scale imaging. *Science* **2006**, *311*, 660–663.

11. Christensen, V.; Guenette, S.; Heymans, J.; Walters, C.; Watson, R.; Zeller, D.; Pauly, D. Hundred-year decline of North Atlantic predatory fishes. *Fish Fish.* **2003**, *4*, 1–24.
12. Drinkwater, K. The response of Atlantic cod *(Gadus morhua)* to future climate change. *ICES J. Mar. Sci. J. Conseil* **2005**, *62*, 1327–1337.
13. Hutchings, J.; Reynolds, J. Marine fish population collapses: Consequences for recovery and extinction risk. *BioScience* **2004**, *54*, 297–309.
14. Ames, E. Atlantic cod stock structure in the Gulf of Maine. *Fisheries* **2004**, *29*, 10–28.
15. Sund, O. Echo sounding in fishery research. *Nature* **1935**, *135*, 953.
16. MacLennan, D.; Simmonds, E.; *Fisheries Acoustics*; Chapman & Hall: London, UK, 1992.
17. Misund, O. Underwater acoustics in marine fisheries and fisheries research. *Rev. Fish Biol. Fisheries* **1997**, *7*, 1–34.
18. Medwin, H.; Clay, C. *Fundamentals of Acoustical Oceanography*; Academic Press: Waltham, MA, USA, 1997.
19. *Fish Stock Assessment 101 Series: Part 1Data Required for Assessing U.S. Fish Stocks*; NOAA Fisheries: Silver Spring, MD, USA, 2012.
20. Gerlotto, F.; Soria, M.; Fréon, P. From two dimensions to three: The use of multibeam sonar for a new approach in fisheries acoustics. *Can. J. Fish. Aquat. Sci.* **1999**, *56*, 6–12.
21. Freon, P.; Misund, O.A. *Dynamics of Pelagic Fish Distribution and Behaviour-Effects on Fisheries and Stock Assessment*; Fishing News Books: Cambridge, UK, 1999.
22. Northeast Fisheries Science Center. *54th Northeast Regional Stock Assessment Workshop (54th SAW): Assessment Report*; Ref Doc. 12-18; Northeast Fisheries Science Center, NOAA: Woods Hole, MA, USA, 2012; p. 600.
23. Løvik, A.; Hovem, J.M. An experimental investigation of swim bladder resonance in fishes. *J. Acoust. Soc. Am.* **1979**, *66*, 850–854.
24. Urick, R.J. *Principles of Underwater Sound*; McGraw Hill: New York, NY, USA, 1983.
25. Bucker, H.P. Wave propagation in a duct with boundary scattering (with application to a surface duct). *J. Acoust. Soc. Am.* **1980**, *68*, 1768–1772.
26. Ivakin, A.N. A unified approach to volume and roughness scattering. *J. Acoust. Soc. Am.* **1998**, *103*, 827–837.
27. Galinde, A.; Donabed, N.; Andrews, M.; Lee, S.; Makris, N.C.; Ratilal, P. Range-dependent waveguide scattering model calibrated for bottom reverberation in a continental shelf environment. *J. Acoust. Soc. Am.* **2008**, *123*, 1270–1281.
28. Morse, P.M.; Ingard, K.U. *Theoretical Acoustics*; Princeton University Press: New Jersey, NJ, USA, 1986.
29. Andrews, M.; Chen, T.; Ratilal, P. Empirical dependence of acoustic transmission scintillation statistics on bandwidth, frequency, and range in New Jersey continental shelf. *J. Acoust. Soc. Am.* **2009**, *125*, 111–124.
30. Gong, Z.; Andrews, M.; Jagannathan, S.; Patel, R.; Jech, J.M.; Makris, N.C.; Ratilal, P. Low-frequency target strength and abundance of shoaling Atlantic herring (*Clupea harengus*) in the Gulf of Maine during the Ocean Acoustic Waveguide Remote Sensing 2006 Experiment. *J. Acoust. Soc. Am.* **2010**, *127*, 104–123.

31. Goff, J.A.; Kraft, B.J.; Mayer, L.A.; Schock, S.G.; Sommerfield, C.K.; Olson, H.C.; Gulick, S.P.S.; Nordfjord, S. Seabed characterization on the New Jersey middle and outer shelf: Correlatability and spatial variability of seafloor sediment properties. *Mar. Geol.* **2004**, *209*, 147–172.
32. Gurshin, C.; Howell, W.; Jech, J. Synoptic acoustic and trawl surveys of spring-spawning Atlantic cod in the Gulf of Maine cod spawning protection area. *Fish. Res.* **2013**, *141*, 44–61.
33. Howell, W. *Synoptic Acoustic and Trawl Surveys to Characterize Biomass and Distribution of the Spring Spawning Aggregations of Atlantic Cod in Lpswich Bay*; FY2009 Northeast Consortium Collaborative Research Award # 111675; Technical Report; 2011.
34. Northeast Fisheries Science Center (NOAA). Northeast (NE) Multispecies Information Sheet Charter/Party and Recreational Fishing. Technical report, National Oceanic And Atmospheric Administration, 2012.
35. Advanced Sampling Technologies Research Group: Surveys, Northeast Fisheries Science Center.
36. Love, R. Resonant acoustic scattering by swim bladder-bearing fish. *J. Acoust. Soc. Am.* **1978**, *64*, 571–580.
37. Jagannathan, S.; Bertsatos, I.; Symonds, D.; Chen, T.; Nia, H.; Jain, A.; Andrews, M.; Gong, Z.; Nero, R.; Ngor, L.; others. Ocean acoustic waveguide remote sensing (OAWRS) of marine ecosystems. *Mar. Ecol. Progr. Series* **2009**, *395*, 137–160.
38. Andrews, M.; Gong, Z.; Ratilal, P. High resolution population density imaging of random scatterers with the matched filtered scattered field variance. *J. Acoust. Soc. Am.* **2009**, *126*, 1057–1068.
39. Collins, M.D. A split-step Pade solution for the parabolic equation method. *J. Acoust. Soc. Am.* **1993**, *93*, 1736–1742.
40. Lawson, G.; Rose, G. The importance of detectability to acoustic surveys of semi-demersal fish. *ICES J. Mar. Sci. J. Conseil* **1999**, *56*, 370–380.
41. Mello, L.G.; Rose, G. Using geostatistics to quantify seasonal distribution and aggregation patterns of fishes: An example of Atlantic cod *(Gadus morhua)*. *Can. J. Fish. Aquat. Sci.* **2005**, *62*, 659–670.
42. van der Kooij, J.; Righton, D.; Strand, E.; Michalsen, K.; Thorsteinsson, V.; Svedäng, H.; Neat, F.C.; Neuenfeldt, S. Life under pressure: Insights from electronic data-storage tags into cod swim bladder function. *ICES J. Mar. Sci. J. Conseil* **2007**, *64*, 1293–1301.
43. Rose, G.; Porter, D. Target-strength studies on Atlantic cod *(Gadus morhua)* in Newfoundland waters. *ICES J. Mar. Sci. J. Consei* **1996**, *53*, 259–265.
44. Arnold, G.; Walker, M. Vertical movements of cod *(Gadus morhua L.)* in the open sea and the hydrostatic function of the swim bladder. *ICES J. Mar. Sci. J. Consei* **1992**, *49*, 357–372.
45. Harden Jones, F.; Scholes, P. Gas secretion and resorption in the swim bladder of the cod *Gadus morhua*. *J. Comp. Physiol. B: Biochem. Syst. Environ. Physiol.* **1985**, *155*, 319–331.
46. Lawson, G.L.; Rose, G.A. Seasonal distribution and movements of coastal cod *(Gadus morhua L.)* in Placentia Bay, Newfoundland. *Fish. Res.* **2000**, *49*, 61–75.
47. Brander, K. *Spawning and Life History Information for North Atlantic Cod Stocks*; Number 205; International Council for the Exploration of the Sea Copenhagen, Denmark, 1994.

48. McQuinn, I.H.; Simard, Y.; Stroud, T.W.; Beaulieu, J.L.; Walsh, S.J. An adaptive, integrated "acoustic-trawl" survey design for Atlantic cod *(Gadus morhua)* with estimation of the acoustic and trawl dead zones. *ICES J. Mar. Sci. J. Consei* **2005**, *62*, 93–106.
49. Gulf of Maine Area Census of Marine Life: Substrates.
50. Rowe, S.; Hutchings, J.A. Sound production by Atlantic cod during spawning. *Trans. Am. Fish. Soc.* **2006**, *135*, 529–538.
51. Fudge, S.B.; Rose, G.A. Passive-and active-acoustic properties of a spawning Atlantic cod *(Gadus morhua)* aggregation. *ICES J. Mar. Sci. J. Consei* **2009**, *66*, 1259–1263.
52. Pitcher, T. *Behaviour of Teleost Fishes*; Springer: Berlin/Heidelberg, Germany, 1992; Volume 7.
53. Brawn, V.M. Sound production by the cod *(Gadus callarias L.)*. *Behaviour* **1961**, *18*, 239–255.
54. Ratilal, P.; Makris, N.C. A unified model for reverberation and submerged target scattering in shallow water. *J. Acoust. Soc. Am.* **2000**, *107*, 2920–2920.
55. Makris, N.C. The effect of saturated transmission scintillation on ocean acoustic intensity measurements. *J. Acoust. Soc. Am.* **1996**, *100*, 769–783.
56. Chen, T.; Ratilal, P.; Makris, N.C. Mean and variance of the forward field propagated through three-dimensional random internal waves in a continental-shelf waveguide. *J. Acoust. Soc. Am.* **2005**, *118*, 3560–3574.
57. Ratilal, P.; Makris, N.C. Mean and covariance of the forward field propagated through a stratified ocean waveguide with three-dimensional random inhomogeneities. *J. Acoust. Soc. Am.* **2005**, *118*, 3532–3559.
58. Lough, R. Essential fish habitat source document: Atlantic cod, *Gadus morhua*, life history and habitat characteristics. *NOAA Tech. Memo. NMFS-NE* **2004**, *190*, 94.
59. Jensen, F.B.; Kuperman, W. A.; Porter, M. B.; Schmidt, H. *Computational Ocean Acoustics*; Springer Science+ Business Media: New York, NY, USA, 2011.
60. Clay, C.S.; Medwin, H. *Acoustical Oceanography*; Wiley: New York, USA, 1977.
61. Brekhovskikh, L.M.; Lysanov, I.P. *Fundamentals of Ocean Acoustics*; Springer: Berlin/Heidelberg, Germany, 2003.
62. National Oceanic and Atmospheric Administration. *Endangered and Threatened Species: Designation of Critical Habitat for Cook Inset Beluga Whale. Proposed Rules*; Federal Register; Technical Report; 2011; pp. 20179–20214.
63. Allen, J.; Peterson, M.; Sharrard, G.; Wright, D.; Todd, S. Radiated noise from commercial ships in the Gulf of Maine: Implications for whale/vessel collisions. *J. Acoust. Soc. Am.* **2012**, *132*, EL229–EL235.
64. Arveson, P.; Vendittis, D. Radiated noise characteristics of a modern cargo ship. *J. Acoust. Soc. Am.* **2000**, *107*, 118–129.
65. Erbe, C. Underwater noise of whale-watching boats and potential effects on killer whales (*Ornicus orca*), based on an acoustic impact model. *Mar. Mamm. Sci.* **2002**, *18*, 394–418.
66. Au, W.W.; Hastings, M.C. *Principles of Marine Bioacoustics*; Springer: Berlin/Heidelberg, Germany, 2008.
67. Medwin, H.; Blue, J.E. *Sounds in the Sea: From Ocean Acoustics to Acoustical Oceanography*; Cambridge University Press: Cambridge, UK, 2005.

68. Richardson, W. J.; Greene Jr., C. R.; Malme, C. I.; Thomson, D.H. *Marine Mammals and Noise*; Academic Press Limited: London, UK, 1995.
69. Division of Marine Fisheries. *Industry-Based Survey for Gulf of Maine Cod, Pilot Study, Appendix G: Ancillary Data: Species of Interest Distribution Maps*; Technical Report; Division of Marine Fisheries, Massachusetts Government: Boston, MA, USA, 2006.
70. Mayo, R.; Terceiro, M. Assessment of 19 Northeast Groundfish Stocks through 2004. In Proceedings of the 2005 Groundfish Assessment Review Meeting (2005 GARM), Northeast Fisheries Science Center, Woods Hole, MA, USA, 15–19 August 2005; pp. 15–19.
71. State of Maine, Maine Department of Marine Resources. *Interjurisdictional Fisheries Resource Monitoring and Assessment: Completion Report*; Grant#NA05NMF4071035; Technical Report; Maine Department of Marine Resources: Augusta, ME, USA, 2010.
72. Rayleigh, B.J.W.S. *The Theory of Sound*; Dover Publications: New York, NY, USA, 1945; Volume I and II.

A. Appendix

Figure A.1. Bathymetric map of (**A**) New Jersey continental shelf and (**B**) Georges Bank showing the location of the fan-shaped patches used for estimating the magnitude squared of the Rayleigh–Born seafloor scattering amplitude. The seafloor scattered field data from these patches was collected along several tracks (black lines) for the respective OAWRS source locations (black diamond) during the (A) 2003 OAWRS experiment for source location 1 (39.0563°N, −73.0365°E) and two receiver tracks extended between (39.08°N, −73.08°E) and (39.07°N, −72.97°E); and (39.09°N, −73.08°E) and (39.06°N, −72.97°E); and (B) 2006 OAWRS experiment for source location 1 (41.8901°N, −68.2134°E), source location 2 (41.9372°N, −68.1046°E), and source location 3 (42.0134°N, −67.829°E) and respective receiver tracks extended between (41.83°N, −68.35°E) and (41.81°N, −68.32°E); (41.98°N, −68.2°E) and (42.05°N, −68.0°E); and (42.05°N, −67.85°E) and (42.1°N, −67.89°E). The gray lines represent depth contours.

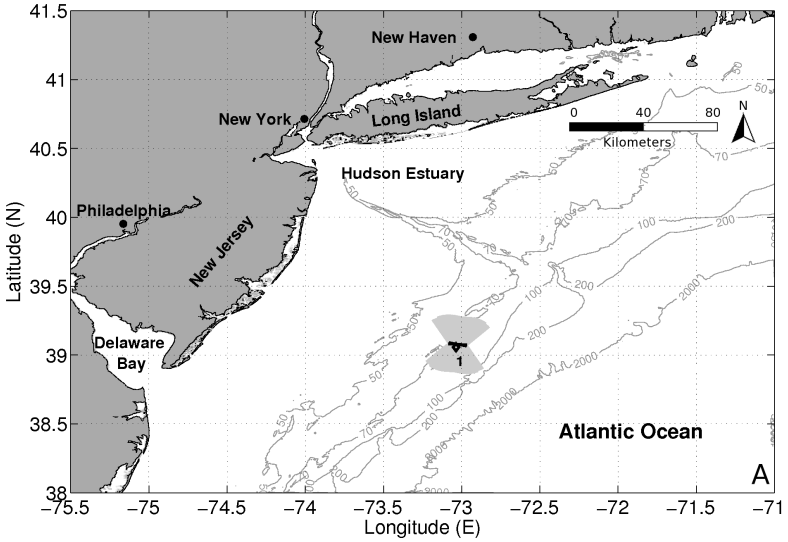

Figure A.1. *Cont.*

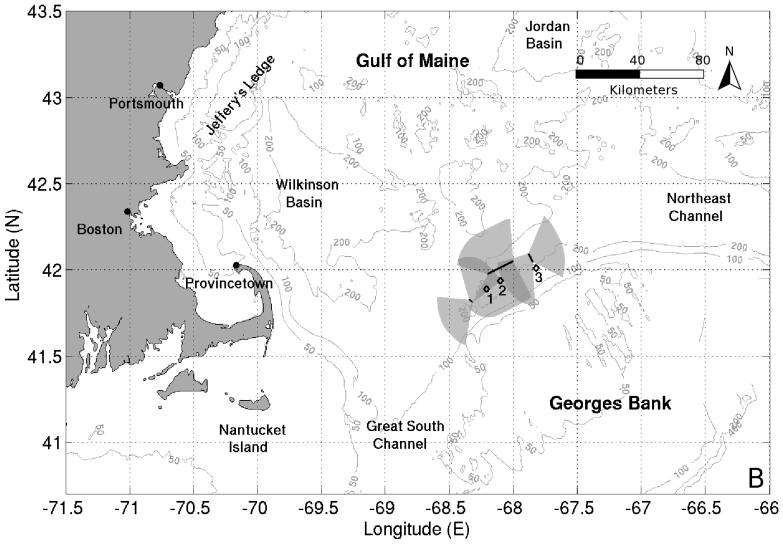

Figure A.2. Comparison between the measured normalized seafloor scattering and the modeled normalized scattered level in the New Jersey continental shelf at (**A**) 415 Hz using 198 radial beams, (**B**) 925 Hz using 187 radial beams and (**C**) 1,325 Hz using 381 radial beams as a function of the total travel time (Section 3.1). The darker regions in the measured scattered field level indicate a higher density of data points. The standard deviation of the measured level (vertical tick marks) is calculated from all the data points that fall within the travel time corresponding to an OAWRS range resolution [9] seconds around a given travel time. The total travel time is the two-way travel time from the source to the seafloor and from the seafloor to the receiver.

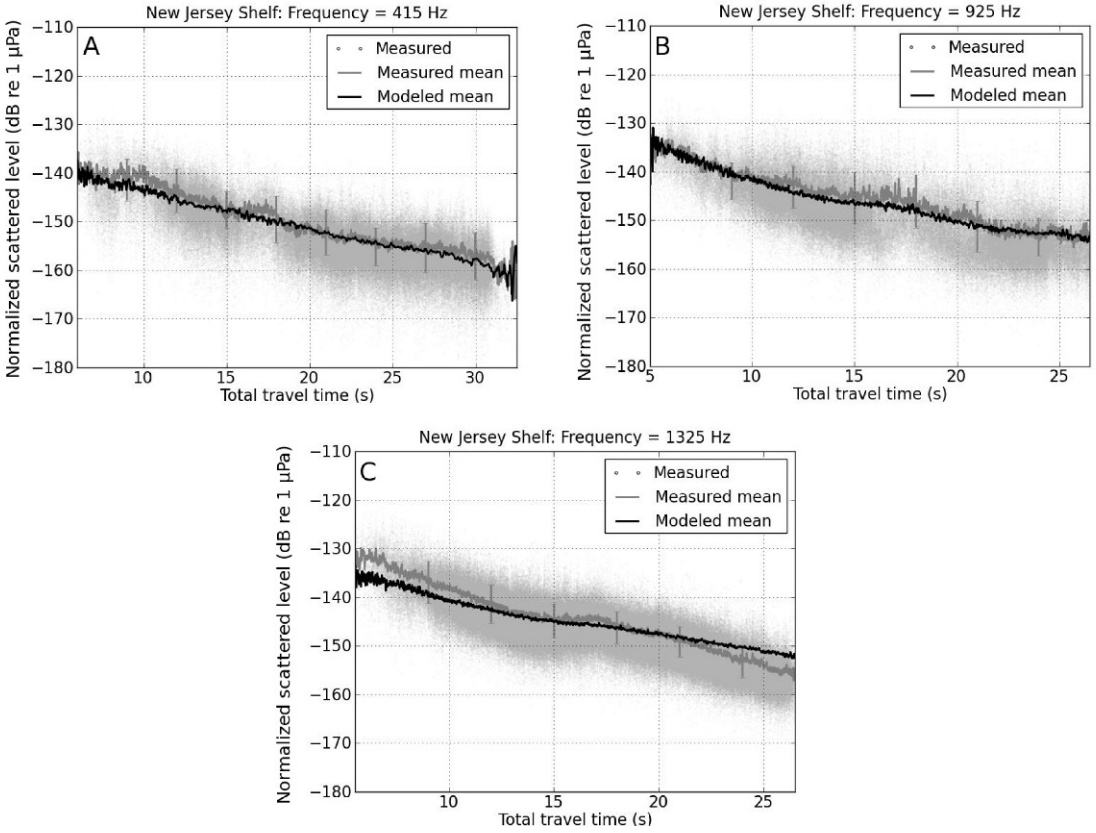

Figure A.3. Comparison between the measured normalized seafloor scattering and the modeled normalized seafloor scattering in the Georges Bank at (**A**) 415 Hz using 410 radial beams, (**B**) 575 Hz using 458 radial beams, (**C**) 735 Hz using 405 radial beams, (**D**) 950 Hz using 408 radial beams and (**E**) 1,125 Hz using 312 radial beams as a function of the total travel time (Section 3.1). The darker regions in the measured scattered level indicate a higher density of data points. The standard deviation of the measured level (vertical tick marks) is calculated from all the data points that fall within the travel time corresponding to an OAWRS range resolution [9] seconds around a given travel time. The total travel time is the two-way travel time from the source to the seafloor and from the seafloor to the receiver.

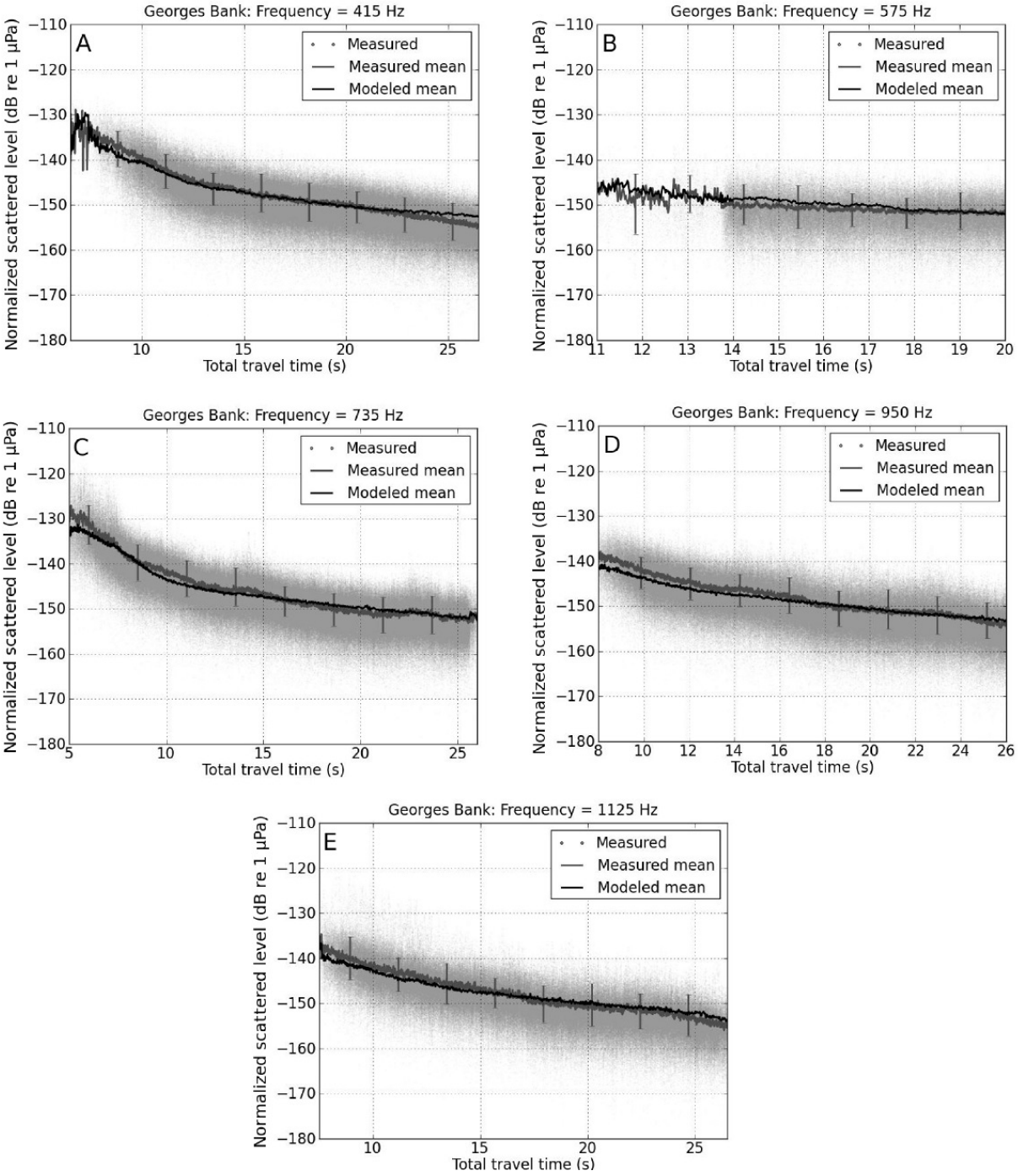

A.1. Analytical Formulation of Rayleigh–Born Volume Scattering from Seafloor

We consider an ocean waveguide consisting of a water layer, located between an air half-space above and a bottom half-space below (Figure A.4). We let (x, y, z) be the coordinates of a Cartesian coordinate system with its origin at the air-water interface and the positive z-axis pointing towards increasing depth in the water column and the seafloor. We place the source at $\mathbf{r}_0$=(x_0, y_0, z_0), the receiver at $\mathbf{r}$ = (x, y, z) and the center of the inhomogeneity at $\mathbf{r}_t$ = (x_t, y_t, z_t).

Figure A.4. (**A**) Geometry for the implementation of the theoretical formulation for the scattered field in a standard Pekeris waveguide of a depth of 100 m for a monostatic point source-receiver located at the mid-water column. The total moments of the scattered field are calculated for a sector of an ocean bottom or seabed patch, extending over range R_t, depth Z_t and azimuth θ_t, containing volume inhomogeneities. The scattered field from the patch then effectively corresponds to the scattered field level measured from a given direction if a receiver array with an angular beamwidth of θ_t is used instead [10]. The sound speed, density and attenuation in the water column and in the sand bottom are c_w, ρ_w, α_w and c_b, ρ_b, α_b, respectively, and (**B**) sound speed profiles measured on the New Jersey continental shelf (gray) are used for the simulations. The solid black line and horizontal tick marks indicate the mean sound speed profile and the standard deviations, respectively [10].

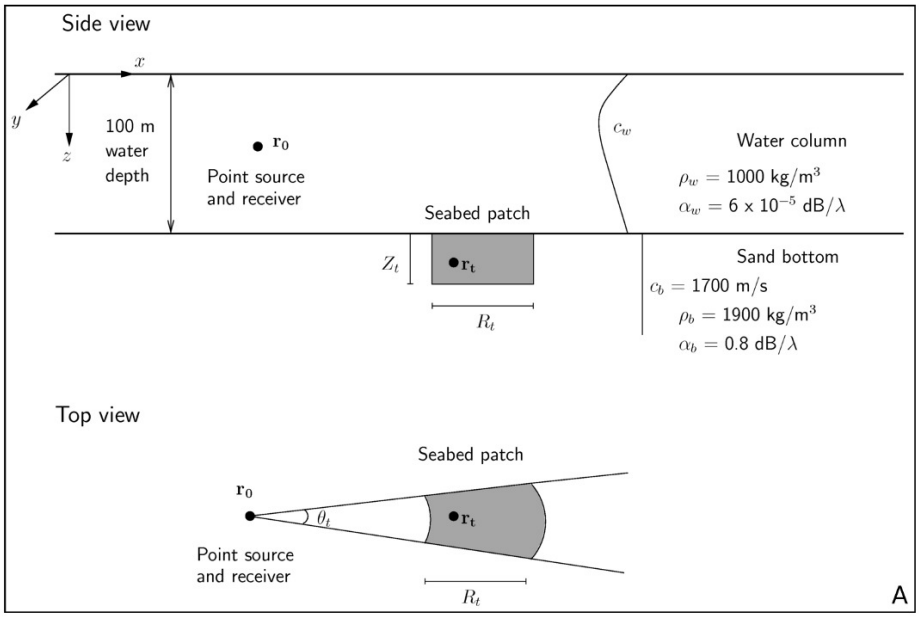

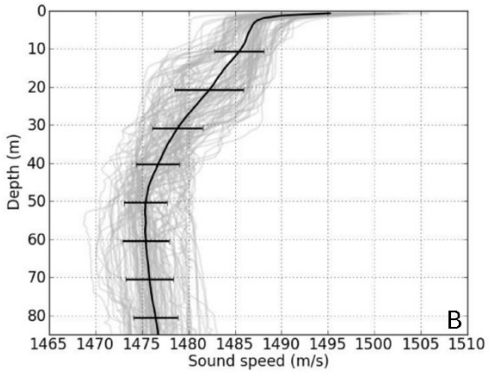

To derive the broadband scattered field from random volume inhomogeneities, we use the Rayleigh–Born approach [26–28,72]. The inhomogeneous Helmholtz equation for a single-frequency, time-independent acoustic field, $\Phi_t(\mathbf{r}_t, f)$, in the presence of volume inhomogeneities is given as:

$$\begin{aligned}\nabla^2\Phi_t(\mathbf{r}_t, f) + k^2\Phi_t(\mathbf{r}_t, f) \\ = -k^2\Gamma_\kappa(\mathbf{r}_t)\Phi_t(\mathbf{r}_t, f) - \nabla\cdot[\Gamma_d(\mathbf{r}_t)\nabla\Phi_t(\mathbf{r}_t, f)]\end{aligned} \tag{A.1}$$

where Γ_κ is the fractional change in medium compressibility:

$$\Gamma_\kappa(\mathbf{r}_t) = \frac{\kappa(\mathbf{r}_t) - \bar{\kappa}}{\bar{\kappa}} \tag{A.2a}$$

Γ_d is the fractional change in medium density:

$$\Gamma_d(\mathbf{r}_t) = \frac{d(\mathbf{r}_t) - \bar{d}}{d(\mathbf{r}_t)} \tag{A.2b}$$

$\bar{\kappa}$ and $\bar{d}$ are the mean compressibility and density in the region, respectively [27,28], f is the frequency, $\omega = 2\pi f$ is the angular frequency, c is the sound speed and $k = \omega/c$ is the acoustic wave number.

Applying Green's theorem [28] to Equation (A.1), we obtain the scattered field, $\Phi_S(\mathbf{r}_S|\mathbf{r}, \mathbf{r}_0, f)$, from inhomogeneities within a volume, V_s, centered on $\mathbf{r}_S$. This region extends along the entire seafloor depth, over the sonar resolution angle in the azimuth and over multiple sonar resolution cells in the range. The scattered field is then given as:

$$\begin{aligned}\Phi_S(\mathbf{r}_S|\mathbf{r}, \mathbf{r}_0, f) = \iiint_{V_S}[k^2\Gamma_\kappa(\mathbf{r}_t)\Phi_t(\mathbf{r}_t, f)G(\mathbf{r}|\mathbf{r}_t, f) \\ + \Gamma_d(\mathbf{r}_t)\nabla\Phi_t(\mathbf{r}_t, f)\cdot\nabla G(\mathbf{r}|\mathbf{r}_t, f)]dV_t\end{aligned} \tag{A.3}$$

Green function $G(\mathbf{r}|\mathbf{r}_t, f)$ describes the propagation from the location of the inhomogeneity to the receiver, and $\Phi_t(\mathbf{r}_t, f)$ is the total field at the location of the inhomogeneity. The total field can be expressed as the sum of the incident field, $\Phi_i(\mathbf{r}_t|\mathbf{r}_0, f)$, and the scattered field, $\Phi_S(\mathbf{r}_t, f)$ [28]:

$$\Phi_t(\mathbf{r}_t, f) = \Phi_i(\mathbf{r}_t|\mathbf{r}_0, f) + \Phi_S(\mathbf{r}_t, f) \tag{A.4}$$

We normalize the source level by letting $\Phi_i(\mathbf{r}_t|\mathbf{r}_0, f) = (4\pi)G(\mathbf{r}_t|\mathbf{r}_0, f)$. For small fluctuations in density and compressibility, we approximate the total field at the location of the inhomogeneity by the incident field using the Born approximation [28], i.e., the total field, Φ_t, can be approximated by the incident field, Φ_i, in Equation (A.3). Then, the scattered field at the receiver is:

$$\begin{aligned}\Phi_S(\mathbf{r}_S|\mathbf{r}, \mathbf{r}_0, f) = (4\pi)\iiint_{V_S}[k^2\Gamma_\kappa(\mathbf{r}_t)G(\mathbf{r}_t|\mathbf{r}_0, f)G(\mathbf{r}|\mathbf{r}_t, f) \\ + \Gamma_d(\mathbf{r}_t)\nabla G(\mathbf{r}_t|\mathbf{r}_0, f)\cdot\nabla G(\mathbf{r}|\mathbf{r}_t, f)]dV_t\end{aligned} \tag{A.5}$$

We derive the scattered field for a source that transmits a broadband waveform, $q(t)$, with Fourier transform $Q(f)$ and bandwidth B around the center frequency, f_c, by applying the matched filter [38] to Equation (A.5). Using Fourier synthesis, the time-domain matched filtered scattered field is:

$$\phi_S(\mathbf{r}_S|\mathbf{r},\mathbf{r}_0,t) = (4\pi)\int_{f_c-B/2}^{f_c+B/2}\iiint_{V_S}[k^2\Gamma_\kappa(\mathbf{r}_t)G(\mathbf{r}_t|\mathbf{r}_0,f)G(\mathbf{r}|\mathbf{r}_t,f) + \Gamma_d(\mathbf{r}_t)\nabla G(\mathbf{r}_t|\mathbf{r}_0,f)\cdot\nabla G(\mathbf{r}|\mathbf{r}_t,f)] \times \frac{1}{\sqrt{E_0}}|Q(f)|^2 e^{-i2\pi f(t-t_M)}\,dV_t\,df \tag{A.6}$$

where t_M represents the time delay of the matched filter and $E_0 = \int |Q(f)|^2 df$ is the source energy.

A.2. Efficient Estimation of Scattering from the Seafloor Field over Wide Areas

We provide expressions for the mean, variance and second moment of the matched filtered scattered field in Appendix A.3. We show that the total broadband seafloor scattered field can be approximated very well by the field at the center frequency of the source signal (Figure A.5) for a typical broadband OAWRS signal [9,10] transmitted in a standard Pekeris waveguide [59] (Figure A.4). This significantly reduces the total computation time of the scattered field over ecosystem scales to a small fraction of the time required to estimate the full field scattered level using the broadband signal. This is especially useful for planning experiments, where actual oceanographic parameters, such as range-dependent sound speed structure, are different from those expected, and experiment parameters, such as source-receiver depth configurations, may need to be modified on-site to optimize detection over long ranges.

We find that the second moment of the broadband field (Equation (A.16)) has a dominant contribution from the variance of the broadband field (Equation (A.17b)), as shown in Figure A.5A. This is expected, because the mean field scattered from diffuse inhomogeneities vanishes in a fluctuating waveguide [54–57]. This variance can be further approximated by terms containing the second moments of seafloor properties (Equation (A.17c)), such as fractional changes in density and compressibility (Figure A.5B). This is because the mean fractional changes in density and compressibility of sandy sediments in the environments we consider (Figure A.1) are known to be small compared to their respective second moments [27]. The broadband variance terms that depend on second moments of seafloor properties can be further approximated by the corresponding terms evaluated at the center frequency (Equations (A.18a) and (A.18c)), as shown in Figure A.5C, when the signal bandwidth is small compared to the center frequency. In addition, we find that this approximation to the variance at the source center frequency can be further decomposed into three terms that are all proportional to each other (Figure A.5D): (a) a monopole scattering term that depends on the variance of fractional changes in seafloor compressibility; (b) a dipole scattering term that depends on the variance of fractional changes in seafloor density; and (c) a cross term that depends on the covariance of fractional changes in seafloor compressibility and density (Equation (A.18d)).

In order to account for random fluctuations in the ocean environment, we vary the sound speed profile with the range [29]. The sound speed profiles used for this environment are selected from the measured sound speed profiles during the 2003 OAWRS experiment in the New Jersey continental shelf [10], and the Green functions are computed using the parabolic equation model, RAM[39]. We consider a monostatic geometry with a single-element source and receiver. The transmitted waveform is a one second-long linear frequency modulated (LFM) pulse [9,10]. The corresponding matched filtered

range resolution, Δr, is then $\Delta r = c/2B$, where c is the reference sound speed and B is the source bandwidth. We use the statistics of fractional changes in density and compressibility as estimated by Galinde *et al*. [27] at the source center frequency of 415 Hz and a bandwidth 50 Hz for the New Jersey continental shelf to model the seafloor-scattered field level.

Figure A.5. The modeled (**A**) total moments of the matched-filtered seafloor scattered field; (**B**) matched-filtered scattered field variance and its components; (**C**) range-averaged matched-filtered scattered field variance compared to the range-averaged variance at the center frequency or time-harmonic approximation; and (**D**) range-averaged variance term $\mathrm{Term}^{\mathrm{TH}}_{<\mathrm{Var}(\Gamma_\kappa),<\mathrm{Var}(\Gamma_d),<\mathrm{Covar}(\Gamma_\kappa,\Gamma_d)}$ compared to its three components, monopole, dipole and cross terms at the center frequency. The source is assumed to be a linear frequency modulated (LFM) pulse centered on 415 Hz and with a bandwidth of 50 Hz. Computations are for a seabed patch extending from 2 km to 20 km in the range, 3° in the azimuth and 10 m in depth, in a Pekeris sand waveguide, as shown in Figure A.4. The cross range resolution of 3° is the typical angular resolution of the OAWRS receiver array [9,10], and the range resolution, $\Delta r = c/2B$, is 15 m for sound speed $c = 1,500$ m/s and OAWRS bandwidth $B = 50$ Hz. The source and receiver are co-located at a depth of 50 m. Detailed derivations of the normalized broadband seafloor scattered field and its moments are given in Appendices A.1–A.3.

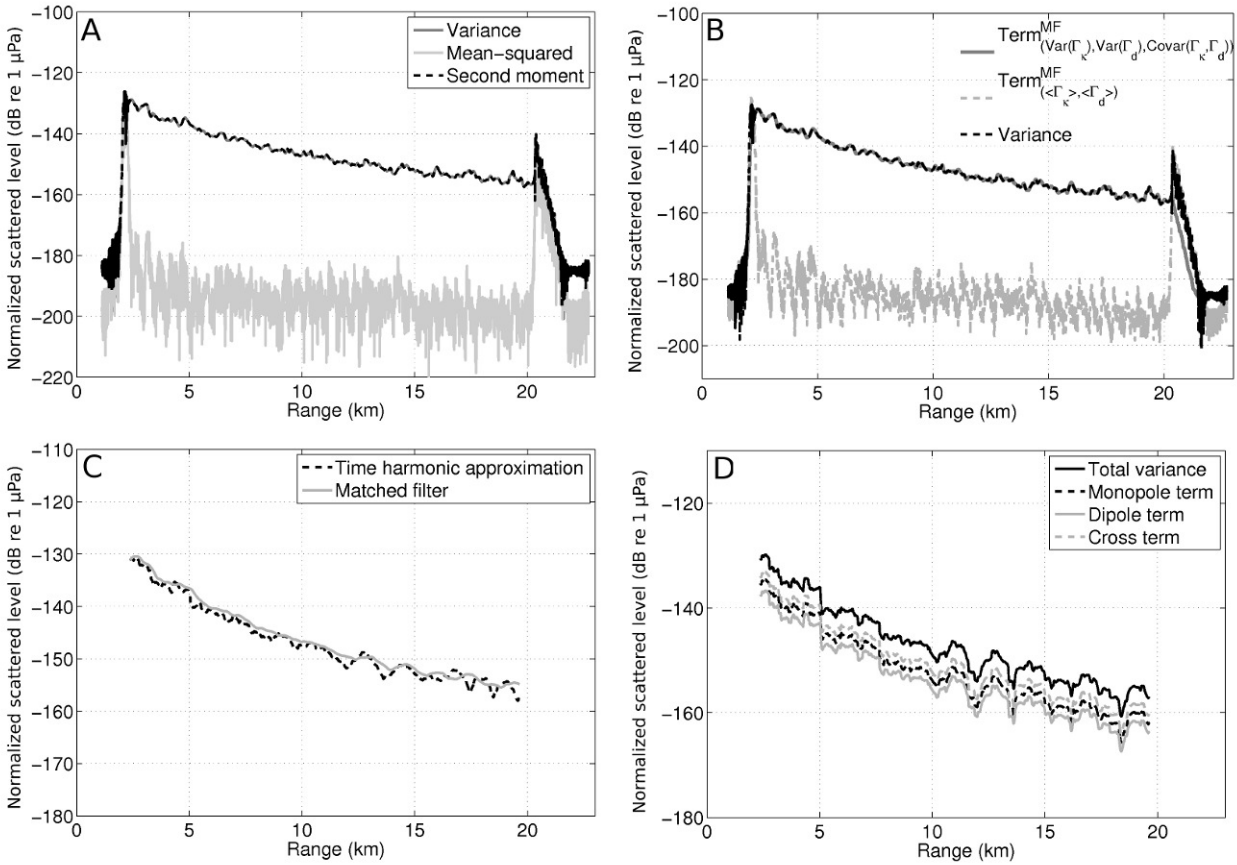

A.3. Full Analytical Expressions for the Total Moments of the Matched Filtered Scattered Field

Here, we derive full analytical expressions for the total moments of the matched filtered scattered field in terms of the statistical moments of fractional changes in compressibility and density and in terms of Green functions and their gradients in a randomly fluctuating ocean waveguide. We assume the bottom inhomogeneities to vary randomly in space, following a stationary random process within the region, V_S, considered. In addition, we assume the fluctuations in the bottom properties to be independent from the fluctuations in the ocean waveguide. Therefore, we can treat the random variables, Γ_κ and Γ_d, as independent from the medium's Green function [27]. Then, following Equation (A.6), the mean matched filtered scattered field can be expressed as:

$$\begin{aligned}\langle \phi_S(\mathbf{r}_S|\mathbf{r},\mathbf{r}_0,t)\rangle = (4\pi)\int_{f_c-B/2}^{f_c+B/2}\iiint_{V_S}[k^2\langle\Gamma_\kappa(\mathbf{r}_t)\rangle\langle G(\mathbf{r}_t|\mathbf{r}_0,f)G(\mathbf{r}|\mathbf{r}_t,f)\rangle \\ +\langle\Gamma_d(\mathbf{r}_t)\rangle\langle\nabla G(\mathbf{r}_t|\mathbf{r}_0,f)\cdot\nabla G(\mathbf{r}|\mathbf{r}_t,f)\rangle] \\ \times\frac{1}{\sqrt{E_0}}|Q(f)|^2 e^{-i2\pi f(t-t_M)}\,dV_t\,df\end{aligned} \tag{A.7}$$

The magnitude of the square of the mean matched filtered scattered field, then, is:

$$\begin{aligned}|\langle\phi_S(\mathbf{r}_S|\mathbf{r},\mathbf{r}_0,t)\rangle|^2 = (4\pi)^2\int_{f_c-B/2}^{f_c+B/2}\int_{f_c-B/2}^{f_c+B/2}\iiint_{V_S}\iiint_{V_S} \\ \times[k^2k'^2\langle\Gamma_\kappa(\mathbf{r}_t)\rangle\langle\Gamma_\kappa(\mathbf{r}'_t)\rangle\langle G(\mathbf{r}_t|\mathbf{r}_0,f)G(\mathbf{r}|\mathbf{r}_t,f)\rangle\langle G^*(\mathbf{r}'_t|\mathbf{r}_0,f')G^*(\mathbf{r}|\mathbf{r}'_t,f')\rangle \\ +\langle\Gamma_d(\mathbf{r}_t)\rangle\langle\Gamma_d(\mathbf{r}'_t)\rangle\langle\nabla G(\mathbf{r}_t|\mathbf{r}_0,f)\cdot\nabla G(\mathbf{r}|\mathbf{r}_t,f)\rangle\langle\nabla G^*(\mathbf{r}'_t|\mathbf{r}_0,f')\cdot\nabla G^*(\mathbf{r}|\mathbf{r}'_t,f')\rangle \\ +k^2\langle\Gamma_\kappa(\mathbf{r}_t)\rangle\langle\Gamma_d(\mathbf{r}'_t)\rangle\langle G(\mathbf{r}_t|\mathbf{r}_0,f)G(\mathbf{r}|\mathbf{r}_t,f)\rangle\langle\nabla G^*(\mathbf{r}'_t|\mathbf{r}_0,f')\cdot\nabla G^*(\mathbf{r}|\mathbf{r}'_t,f')\rangle \\ +k'^2\langle\Gamma_\kappa(\mathbf{r}'_t)\rangle\langle\Gamma_d(\mathbf{r}_t)\rangle\langle G^*(\mathbf{r}'_t|\mathbf{r}_0,f')G^*(\mathbf{r}|\mathbf{r}'_t,f')\rangle\langle\nabla G(\mathbf{r}_t|\mathbf{r}_0,f)\cdot\nabla G(\mathbf{r}|\mathbf{r}_t,f)\rangle] \\ \times\frac{1}{E_0}|Q(f)|^2|Q(f')|^2 e^{-i2\pi(f-f')(t-t_M)}\,dV_t\,dV'_t\,df\,df'\end{aligned} \tag{A.8}$$

and the second moment of the scattered field is:

$$\begin{aligned}\langle|\phi_S(\mathbf{r}_S|\mathbf{r},\mathbf{r}_0,t)|^2\rangle = \langle\phi_S(\mathbf{r}_S|\mathbf{r},\mathbf{r}_0,t_M)\phi_S^*(\mathbf{r}_S|\mathbf{r},\mathbf{r}_0,t_M)\rangle \\ =\langle(4\pi)\int_{f_c-B/2}^{f_c+B/2}\iiint_{V_S}[k^2\Gamma_\kappa(\mathbf{r}_t)G(\mathbf{r}_t|\mathbf{r}_0,f)G(\mathbf{r}|\mathbf{r}_t,f) \\ +\Gamma_d(\mathbf{r}_t)\nabla G(\mathbf{r}_t|\mathbf{r}_0,f)\cdot\nabla G(\mathbf{r}|\mathbf{r}_t,f)]\times\frac{1}{\sqrt{E_0}}|Q(f)|^2 e^{-i2\pi f(t-t_M)}\,dV_t\,df \\ \times(4\pi)\int_{f_c-B/2}^{f_c+B/2}\iiint_{V_S}[k'^2\Gamma_\kappa(\mathbf{r}'_t)G^*(\mathbf{r}'_t|\mathbf{r}_0,f')G^*(\mathbf{r}|\mathbf{r}'_t,f') \\ +\Gamma_d(\mathbf{r}'_t)\nabla G^*(\mathbf{r}'_t|\mathbf{r}_0,f')\cdot\nabla G^*(\mathbf{r}|\mathbf{r}'_t,f')]\times\frac{1}{\sqrt{E_0}}|Q(f')|^2 e^{-i2\pi f'(t-t_M)}\,dV'_t\,df'\rangle\end{aligned} \tag{A.9}$$

which can be written as:

$$\begin{aligned}
&\langle|\phi_S(\mathbf{r}_S|\mathbf{r},\mathbf{r}_0,t)|^2\rangle \qquad (A.10)\\
&= (4\pi)^2 \int_{f_c-B/2}^{f_c+B/2}\int_{f_c-B/2}^{f_c+B/2}\iiint_{V_S}\iiint_{V_S}\\
&[k^2k'^2\langle\Gamma_\kappa(\mathbf{r}_t)\Gamma_\kappa(\mathbf{r}'_t)\rangle\langle G(\mathbf{r}_t|\mathbf{r}_0,f)G(\mathbf{r}|\mathbf{r}_t,f)G^*(\mathbf{r}'_t|\mathbf{r}_0,f')G^*(\mathbf{r}|\mathbf{r}'_t,f')\rangle\\
&+\langle\Gamma_d(\mathbf{r}_t)\Gamma_d(\mathbf{r}'_t)\rangle\langle\nabla G(\mathbf{r}_t|\mathbf{r}_0,f)\cdot\nabla G(\mathbf{r}|\mathbf{r}_t,f)\times\nabla G^*(\mathbf{r}'_t|\mathbf{r}_0,f')\cdot\nabla G^*(\mathbf{r}|\mathbf{r}'_t,f')\rangle\\
&+k^2\langle\Gamma_\kappa(\mathbf{r}_t)\Gamma_d(\mathbf{r}'_t)\rangle\langle G(\mathbf{r}_t|\mathbf{r}_0,f)G(\mathbf{r}|\mathbf{r}_t,f)\nabla G^*(\mathbf{r}'_t|\mathbf{r}_0,f')\cdot\nabla G^*(\mathbf{r}|\mathbf{r}'_t,f')\rangle\\
&+k'^2\langle\Gamma_\kappa(\mathbf{r}'_t)\Gamma_d(\mathbf{r}_t)\rangle\langle G^*(\mathbf{r}'_t|\mathbf{r}_0,f')G^*(\mathbf{r}|\mathbf{r}'_t,f')\nabla G(\mathbf{r}_t|\mathbf{r}_0,f)\cdot\nabla G(\mathbf{r}|\mathbf{r}_t,f)\rangle]\\
&\times\frac{1}{E_0}|Q(f)|^2|Q(f')|^2e^{-i2\pi(f-f')(t-t_M)}\,dV_t\,dV'_t\,df\,df'
\end{aligned}$$

To model the statistics of the density and compressibility variations, we use a delta correlation function and assume the parameters to be correlated in all three dimensions within a coherence volume [27]; let:

$$\begin{aligned}
&\langle\Gamma_\kappa(\mathbf{r}_t)\Gamma_\kappa(\mathbf{r}'_t)\rangle \qquad (A.11)\\
&= V_c(\mathbf{r}_S,z_t)[\langle\Gamma^2_\kappa(\mathbf{r}_t)\rangle-|\langle\Gamma_\kappa(\mathbf{r}_t)\rangle|^2]\delta(\mathbf{r}_t-\mathbf{r}'_t)+\langle\Gamma_\kappa(\mathbf{r}_t)\rangle\langle\Gamma_\kappa(\mathbf{r}'_t)\rangle\\
&= V_c(\mathbf{r}_S,z_t)\mathrm{Var}(\Gamma_\kappa(\mathbf{r}_t)\delta(\mathbf{r}_t-\mathbf{r}'_t)+\langle\Gamma_\kappa(\mathbf{r}_t)\rangle\langle\Gamma_\kappa(\mathbf{r}'_t)\rangle
\end{aligned}$$

Similarly:

$$\begin{aligned}
&\langle\Gamma_d(\mathbf{r}_t)\Gamma_d(\mathbf{r}'_t)\rangle \qquad (A.12)\\
&= V_c(\mathbf{r}_S,z_t)\mathrm{Var}(\Gamma_d(\mathbf{r}_t))\delta(\mathbf{r}_t-\mathbf{r}'_t)+\langle\Gamma_d(\mathbf{r}_t)\rangle\langle\Gamma_d(\mathbf{r}'_t)\rangle\\
&\langle\Gamma_\kappa(\mathbf{r}_t)\Gamma_d(\mathbf{r}'_t)\rangle \qquad (A.13)\\
&= V_c(\mathbf{r}_S,z_t)\mathrm{Covar}(\Gamma_\kappa(\mathbf{r}_t),\Gamma_d(\mathbf{r}_t))\delta(\mathbf{r}_t-\mathbf{r}'_t)+\langle\Gamma_\kappa(\mathbf{r}_t)\rangle\langle\Gamma_d(\mathbf{r}'_t)\rangle\\
&\langle\Gamma_\kappa(\mathbf{r}'_t)\Gamma_d(\mathbf{r}_t)\rangle \qquad (A.14)\\
&= V_c(\mathbf{r}_S,z_t)\mathrm{Covar}(\Gamma_\kappa(\mathbf{r}_t),\Gamma_d(\mathbf{r}_t))\delta(\mathbf{r}_t-\mathbf{r}'_t)+\langle\Gamma_\kappa(\mathbf{r}'_t)\rangle\langle\Gamma_d(\mathbf{r}_t)\rangle
\end{aligned}$$

Then, Equation (A.10) becomes:

$$\begin{aligned}
&\langle|\phi_S(\mathbf{r}_S|\mathbf{r},\mathbf{r}_0,t)|^2\rangle \qquad (A.15)\\
&= (4\pi)^2\int_{f_c-B/2}^{f_c+B/2}\int_{f_c-B/2}^{f_c+B/2}\iiint_{V_S}\iiint_{V_S}V_c(\mathbf{r}_S,z_t)\\
&\times[k^2k'^2\mathrm{Var}(\Gamma_\kappa)\delta(\mathbf{r}_t-\mathbf{r}'_t)\langle G(\mathbf{r}_t|\mathbf{r}_0,f)G(\mathbf{r}|\mathbf{r}_t,f)G^*(\mathbf{r}'_t|\mathbf{r}_0,f')G^*(\mathbf{r}|\mathbf{r}'_t,f')\rangle\\
&+\mathrm{Var}(\Gamma_d)\delta(\mathbf{r}_t-\mathbf{r}'_t)\langle\nabla G(\mathbf{r}_t|\mathbf{r}_0,f)\cdot\nabla G(\mathbf{r}|\mathbf{r}_t,f)\times\nabla G^*(\mathbf{r}'_t|\mathbf{r}_0,f')\cdot\nabla G^*(\mathbf{r}|\mathbf{r}'_t,f')\rangle\\
&+k^2\mathrm{Covar}(\Gamma_\kappa,\Gamma_d)\delta(\mathbf{r}_t-\mathbf{r}'_t)\langle G(\mathbf{r}_t|\mathbf{r}_0,f)G(\mathbf{r}|\mathbf{r}_t,f)\nabla G^*(\mathbf{r}'_t|\mathbf{r}_0,f')\cdot\nabla G^*(\mathbf{r}|\mathbf{r}'_t,f')\rangle\\
&+k'^2\mathrm{Covar}(\Gamma_\kappa,\Gamma_d)\delta(\mathbf{r}_t-\mathbf{r}'_t)\langle G^*(\mathbf{r}'_t|\mathbf{r}_0,f')G^*(\mathbf{r}|\mathbf{r}'_t,f')\nabla G(\mathbf{r}_t|\mathbf{r}_0,f)\cdot\nabla G(\mathbf{r}|\mathbf{r}_t,f)\rangle]\\
&\times\frac{1}{E_0}|Q(f)|^2|Q(f')|^2e^{-i2\pi(f-f')(t-t_M)}\,dV_t\,dV'_t\,df\,df'+
\end{aligned}$$

$$
\begin{aligned}
&+ (4\pi)^2 \int_{f_c-B/2}^{f_c+B/2} \int_{f_c-B/2}^{f_c+B/2} \iiint_{V_S} \iiint_{V_S} \\
&\quad \times [k^2 k'^2 \langle \Gamma_\kappa(\mathbf{r}_t) \rangle \langle \Gamma_\kappa(\mathbf{r}'_t) \rangle \langle G(\mathbf{r}_t|\mathbf{r}_0, f) G(\mathbf{r}|\mathbf{r}_t, f) G^*(\mathbf{r}'_t|\mathbf{r}_0, f') G^*(\mathbf{r}|\mathbf{r}'_t, f') \rangle \\
&\quad + \langle \Gamma_d(\mathbf{r}_t) \rangle \langle \Gamma_d(\mathbf{r}'_t) \rangle \langle \nabla G(\mathbf{r}_t|\mathbf{r}_0, f) \cdot \nabla G(\mathbf{r}|\mathbf{r}_t, f) \times \nabla G^*(\mathbf{r}'_t|\mathbf{r}_0, f') \cdot \nabla G^*(\mathbf{r}|\mathbf{r}'_t, f') \rangle \\
&\quad + k^2 \langle \Gamma_\kappa(\mathbf{r}_t) \rangle \langle \Gamma_d(\mathbf{r}'_t) \rangle \langle G(\mathbf{r}_t|\mathbf{r}_0, f) G(\mathbf{r}|\mathbf{r}_t, f) \nabla G^*(\mathbf{r}'_t|\mathbf{r}_0, f') \cdot \nabla G^*(\mathbf{r}|\mathbf{r}'_t, f') \rangle \\
&\quad + k'^2 \langle \Gamma_\kappa(\mathbf{r}'_t) \rangle \langle \Gamma_d(\mathbf{r}_t) \rangle \langle G^*(\mathbf{r}'_t|\mathbf{r}_0, f') G^*(\mathbf{r}|\mathbf{r}'_t, f') \nabla G(\mathbf{r}_t|\mathbf{r}_0, f) \cdot \nabla G(\mathbf{r}|\mathbf{r}_t, f) \rangle] \\
&\quad \times \frac{1}{E_0} |Q(f)|^2 |Q(f')|^2 e^{-i2\pi(f-f')(t-t_M)} \, dV_t \, dV'_t \, df \, df'
\end{aligned}
$$

After integrating one of the delta functions over the volume, V_S, in the first term of Equation (A.15), the full expression for the matched filtered total second moment is:

$$
\begin{aligned}
&\langle |\phi_S(\mathbf{r}_S|\mathbf{r}, \mathbf{r}_0, t)|^2 \rangle \qquad \text{(A.16)} \\
&= (4\pi)^2 \int_{f_c-B/2}^{f_c+B/2} \int_{f_c-B/2}^{f_c+B/2} \iiint_{V_S} V_c(\mathbf{r}_S, z_t) \\
&\quad \times [k^2 k'^2 \text{Var}(\Gamma_\kappa) \langle G(\mathbf{r}_t|\mathbf{r}_0, f) G(\mathbf{r}|\mathbf{r}_t, f) G^*(\mathbf{r}_t|\mathbf{r}_0, f') G^*(\mathbf{r}|\mathbf{r}_t, f') \rangle \\
&\quad + \text{Var}(\Gamma_d) \langle \nabla G(\mathbf{r}_t|\mathbf{r}_0, f) \cdot \nabla G(\mathbf{r}|\mathbf{r}_t, f) \times \nabla G^*(\mathbf{r}_t|\mathbf{r}_0, f') \cdot \nabla G^*(\mathbf{r}|\mathbf{r}_t, f') \rangle \\
&\quad + k^2 \text{Covar}(\Gamma_\kappa, \Gamma_d) \langle G(\mathbf{r}_t|\mathbf{r}_0, f) G(\mathbf{r}|\mathbf{r}_t, f) \nabla G^*(\mathbf{r}_t|\mathbf{r}_0, f') \cdot \nabla G^*(\mathbf{r}|\mathbf{r}_t, f') \rangle \\
&\quad + k'^2 \text{Covar}(\Gamma_\kappa, \Gamma_d) \langle G^*(\mathbf{r}_t|\mathbf{r}_0, f') G^*(\mathbf{r}|\mathbf{r}_t, f') \nabla G(\mathbf{r}_t|\mathbf{r}_0, f) \cdot \nabla G(\mathbf{r}|\mathbf{r}_t, f) \rangle] \\
&\quad \times \frac{1}{E_0} |Q(f)|^2 |Q(f')|^2 e^{-i2\pi(f-f')(t-t_M)} \, dV_t \, df \, df' + \\
&+ (4\pi)^2 \int_{f_c-B/2}^{f_c+B/2} \int_{f_c-B/2}^{f_c+B/2} \iiint_{V_S} \iiint_{V_S} \\
&\quad \times [k^2 k'^2 \langle \Gamma_\kappa(\mathbf{r}_t) \rangle \langle \Gamma_\kappa(\mathbf{r}'_t) \rangle \langle G(\mathbf{r}_t|\mathbf{r}_0, f) G(\mathbf{r}|\mathbf{r}_t, f) G^*(\mathbf{r}'_t|\mathbf{r}_0, f') G^*(\mathbf{r}|\mathbf{r}'_t, f') \rangle \\
&\quad + \langle \Gamma_d(\mathbf{r}_t) \rangle \langle \Gamma_d(\mathbf{r}'_t) \rangle \langle \nabla G(\mathbf{r}_t|\mathbf{r}_0, f) \cdot \nabla G(\mathbf{r}|\mathbf{r}_t, f) \times \nabla G^*(\mathbf{r}'_t|\mathbf{r}_0, f') \cdot \nabla G^*(\mathbf{r}|\mathbf{r}'_t, f') \rangle \\
&\quad + k^2 \langle \Gamma_\kappa(\mathbf{r}_t) \rangle \langle \Gamma_d(\mathbf{r}'_t) \rangle \langle G(\mathbf{r}_t|\mathbf{r}_0, f) G(\mathbf{r}|\mathbf{r}_t, f) \nabla G^*(\mathbf{r}'_t|\mathbf{r}_0, f') \cdot \nabla G^*(\mathbf{r}|\mathbf{r}'_t, f') \rangle \\
&\quad + k'^2 \langle \Gamma_\kappa(\mathbf{r}'_t) \rangle \langle \Gamma_d(\mathbf{r}_t) \rangle \langle G^*(\mathbf{r}'_t|\mathbf{r}_0, f') G^*(\mathbf{r}|\mathbf{r}'_t, f') \nabla G(\mathbf{r}_t|\mathbf{r}_0, f) \cdot \nabla G(\mathbf{r}|\mathbf{r}_t, f) \rangle] \\
&\quad \times \frac{1}{E_0} |Q(f)|^2 |Q(f')|^2 e^{-i2\pi(f-f')(t-t_M)} \, dV_t \, dV'_t \, df \, df'
\end{aligned}
$$

The total variance can be expressed in terms of the total second moment and the squared of the mean field as:

$$
\text{Var}(\phi_S(\mathbf{r}_S|\mathbf{r}, \mathbf{r}_0, t)) = \langle |\phi_S(\mathbf{r}_S|\mathbf{r}, \mathbf{r}_0, t)|^2 \rangle - |\langle \phi_S(\mathbf{r}_S|\mathbf{r}, \mathbf{r}_0, t) \rangle|^2 \qquad \text{(A.17a)}
$$

which can be further expanded as:

$$
\begin{aligned}
&\text{Var}(\phi_S(\mathbf{r}_S|\mathbf{r}, \mathbf{r}_0, t)) \qquad \text{(A.17b)} \\
&= (4\pi)^2 \int_{f_c-B/2}^{f_c+B/2} \int_{f_c-B/2}^{f_c+B/2} \iiint_{V_S} V_c(\mathbf{r}_S, z_t) \\
&\quad \times [k^2 k'^2 \text{Var}(\Gamma_\kappa) \langle G(\mathbf{r}_t|\mathbf{r}_0, f) G(\mathbf{r}|\mathbf{r}_t, f) G^*(\mathbf{r}_t|\mathbf{r}_0, f') G^*(\mathbf{r}|\mathbf{r}_t, f') \rangle
\end{aligned}
$$

$$
\begin{aligned}
&+ \mathrm{Var}(\Gamma_d)\langle \nabla G(\mathbf{r}_t|\mathbf{r}_0,f)\cdot\nabla G(\mathbf{r}|\mathbf{r}_t,f)\times\nabla G^*(\mathbf{r}_t|\mathbf{r}_0,f')\cdot\nabla G^*(\mathbf{r}|\mathbf{r}_t,f')\rangle \\
&+ k^2\mathrm{Covar}(\Gamma_\kappa,\Gamma_d)\langle G(\mathbf{r}_t|\mathbf{r}_0,f)G(\mathbf{r}|\mathbf{r}_t,f)\nabla G^*(\mathbf{r}_t|\mathbf{r}_0,f')\cdot\nabla G^*(\mathbf{r}|\mathbf{r}_t,f')\rangle \\
&+ k'^2\mathrm{Covar}(\Gamma_\kappa,\Gamma_d)\langle G^*(\mathbf{r}_t|\mathbf{r}_0,f')G^*(\mathbf{r}|\mathbf{r}_t,f')\nabla G(\mathbf{r}_t|\mathbf{r}_0,f)\cdot\nabla G(\mathbf{r}|\mathbf{r}_t,f)\rangle] \\
&\times \frac{1}{E_0}|Q(f)|^2|Q(f')|^2 e^{-i2\pi(f-f')(t-t_M)}\,dV_t\,df\,df' \\
+ (4\pi)^2 &\int_{f_c-B/2}^{f_c+B/2}\int_{f_c-B/2}^{f_c+B/2}\iiint_{V_S}\iiint_{V_S} \\
&\times [k^2k'^2\langle\Gamma_\kappa(\mathbf{r}_t)\rangle\langle\Gamma_\kappa(\mathbf{r}'_t)\rangle\langle G(\mathbf{r}_t|\mathbf{r}_0,f)G(\mathbf{r}|\mathbf{r}_t,f)G^*(\mathbf{r}'_t|\mathbf{r}_0,f')G^*(\mathbf{r}|\mathbf{r}'_t,f')\rangle \\
&+ \langle\Gamma_d(\mathbf{r}_t)\rangle\langle\Gamma_d(\mathbf{r}'_t)\rangle\langle\nabla G(\mathbf{r}_t|\mathbf{r}_0,f)\cdot\nabla G(\mathbf{r}|\mathbf{r}_t,f)\times\nabla G^*(\mathbf{r}'_t|\mathbf{r}_0,f')\cdot\nabla G^*(\mathbf{r}|\mathbf{r}'_t,f')\rangle \\
&+ k^2\langle\Gamma_\kappa(\mathbf{r}_t)\rangle\langle\Gamma_d(\mathbf{r}'_t)\rangle\langle G(\mathbf{r}_t|\mathbf{r}_0,f)G(\mathbf{r}|\mathbf{r}_t,f)\nabla G^*(\mathbf{r}'_t|\mathbf{r}_0,f')\cdot\nabla G^*(\mathbf{r}|\mathbf{r}'_t,f')\rangle \\
&+ k'^2\langle\Gamma_\kappa(\mathbf{r}'_t)\rangle\langle\Gamma_d(\mathbf{r}_t)\rangle\langle G^*(\mathbf{r}'_t|\mathbf{r}_0,f')G^*(\mathbf{r}|\mathbf{r}'_t,f')\nabla G(\mathbf{r}_t|\mathbf{r}_0,f)\cdot\nabla G(\mathbf{r}|\mathbf{r}_t,f)\rangle] \\
&\times \frac{1}{E_0}|Q(f)|^2|Q(f')|^2 e^{-i2\pi(f-f')(t-t_M)}\,dV_t\,dV'_t\,df\,df' \\
- (4\pi)^2 &\int_{f_c-B/2}^{f_c+B/2}\int_{f_c-B/2}^{f_c+B/2}\iiint_{V_S}\iiint_{V_S} \\
&\times [k^2k'^2\langle\Gamma_\kappa(\mathbf{r}_t)\rangle\langle\Gamma_\kappa(\mathbf{r}'_t)\rangle\langle G(\mathbf{r}_t|\mathbf{r}_0,f)G(\mathbf{r}|\mathbf{r}_t,f)\rangle\langle G^*(\mathbf{r}'_t|\mathbf{r}_0,f')G^*(\mathbf{r}|\mathbf{r}'_t,f')\rangle \\
&+ \langle\Gamma_d(\mathbf{r}_t)\rangle\langle\Gamma_d(\mathbf{r}'_t)\rangle\langle\nabla G(\mathbf{r}_t|\mathbf{r}_0,f)\cdot\nabla G(\mathbf{r}|\mathbf{r}_t,f)\rangle\langle\nabla G^*(\mathbf{r}'_t|\mathbf{r}_0,f')\cdot\nabla G^*(\mathbf{r}|\mathbf{r}'_t,f')\rangle \\
&+ k^2\langle\Gamma_\kappa(\mathbf{r}_t)\rangle\langle\Gamma_d(\mathbf{r}'_t)\rangle\langle G(\mathbf{r}_t|\mathbf{r}_0,f)G(\mathbf{r}|\mathbf{r}_t,f)\rangle\langle\nabla G^*(\mathbf{r}'_t|\mathbf{r}_0,f')\cdot\nabla G^*(\mathbf{r}|\mathbf{r}'_t,f')\rangle \\
&+ k'^2\langle\Gamma_\kappa(\mathbf{r}'_t)\rangle\langle\Gamma_d(\mathbf{r}_t)\rangle\langle G^*(\mathbf{r}'_t|\mathbf{r}_0,f')G^*(\mathbf{r}|\mathbf{r}'_t,f')\rangle\langle\nabla G(\mathbf{r}_t|\mathbf{r}_0,f)\cdot\nabla G(\mathbf{r}|\mathbf{r}_t,f)\rangle] \\
&\times \frac{1}{E_0}|Q(f)|^2|Q(f')|^2 e^{-i2\pi(f-f')(t-t_M)}\,dV_t\,dV'_t\,df\,df'. \\
&= \mathrm{Term}^{\mathrm{MF}}_{(\mathrm{Var}(\Gamma_\kappa),\mathrm{Var}(\Gamma_d),\mathrm{Covar}(\Gamma_\kappa,\Gamma_d))} + \mathrm{Term}^{\mathrm{MF}}_{(<\Gamma_\kappa>,<\Gamma_d>)}
\end{aligned}
$$

Although Equation (A.17b) represents the full expression for the matched filtered total variance, we show in Section A.2 that the last integral term of the variance Equation (A.17b) is negligible, so that the variance can be approximated by the first integral term as:

$$
\begin{aligned}
&\mathrm{Var}(\phi_S(\mathbf{r}_S|\mathbf{r},\mathbf{r}_0,t)) \qquad\qquad (A.17c)\\
&= (4\pi)^2\int_{f_c-B/2}^{f_c+B/2}\int_{f_c-B/2}^{f_c+B/2}\iiint_{V_S} V_c(\mathbf{r}_S,z_t) \\
&\quad\times [k^2k'^2\mathrm{Var}(\Gamma_\kappa)\langle G(\mathbf{r}_t|\mathbf{r}_0,f)G(\mathbf{r}|\mathbf{r}_t,f)G^*(\mathbf{r}_t|\mathbf{r}_0,f')G^*(\mathbf{r}|\mathbf{r}_t,f')\rangle \\
&\quad+ \mathrm{Var}(\Gamma_d)\langle\nabla G(\mathbf{r}_t|\mathbf{r}_0,f)\cdot\nabla G(\mathbf{r}|\mathbf{r}_t,f)\times\nabla G^*(\mathbf{r}_t|\mathbf{r}_0,f')\cdot\nabla G^*(\mathbf{r}|\mathbf{r}_t,f')\rangle \\
&\quad+ k^2\mathrm{Covar}(\Gamma_\kappa,\Gamma_d)\langle G(\mathbf{r}_t|\mathbf{r}_0,f)G(\mathbf{r}|\mathbf{r}_t,f)\nabla G^*(\mathbf{r}_t|\mathbf{r}_0,f')\cdot\nabla G^*(\mathbf{r}|\mathbf{r}_t,f')\rangle \\
&\quad+ k'^2\mathrm{Covar}(\Gamma_\kappa,\Gamma_d)\langle G^*(\mathbf{r}_t|\mathbf{r}_0,f')G^*(\mathbf{r}|\mathbf{r}_t,f')\nabla G(\mathbf{r}_t|\mathbf{r}_0,f)\cdot\nabla G(\mathbf{r}|\mathbf{r}_t,f)\rangle] \\
&\quad\times\frac{1}{E_0}|Q(f)|^2|Q(f')|^2 e^{-i2\pi(f-f')(t-t_M)}\,dV_t\,df\,df'
\end{aligned}
$$

A.4. Time Harmonic Approximation to the Matched Filtered Scattered Intensity

In this section, we present a computationally efficient approximation to the matched filtered scattered intensity derived in Appendix A.3. Starting with Equation (A.5) for the time harmonic scattered field,

where V_S now represents the resolution cell of the imaging system, we follow a procedure similar to the one used in Appendix A.3 and find that the time harmonic total variance is:

$$\begin{aligned}
&\mathrm{Var}(\Phi_S(\mathbf{r}_S|\mathbf{r},\mathbf{r}_0,f)) && \text{(A.18a)}\\
&= (4\pi)^2 \iiint_{V_S} V_c(\mathbf{r}_S,z_t)\\
&\quad \times [k^4\mathrm{Var}(\Gamma_\kappa)\langle|G(\mathbf{r}_t|\mathbf{r}_0,f)|^2|G(\mathbf{r}|\mathbf{r}_t,f)|^2\rangle\\
&\quad + \mathrm{Var}(\Gamma_d)\langle|\nabla G(\mathbf{r}_t|\mathbf{r}_0,f)\cdot\nabla G(\mathbf{r}|\mathbf{r}_t,f)|^2\rangle\\
&\quad + k^2\mathrm{Covar}(\Gamma_\kappa,\Gamma_d)\langle 2\Re\{G(\mathbf{r}_t|\mathbf{r}_0,f)G(\mathbf{r}|\mathbf{r}_t,f)\nabla G^*(\mathbf{r}_t|\mathbf{r}_0,f)\cdot\nabla G^*(\mathbf{r}|\mathbf{r}_t,f)\}\rangle]\,dV_t\\
&+ (4\pi)^2 \iiint_{V_S}\iiint_{V_S} [k^4\langle\Gamma_\kappa(\mathbf{r}_t)\rangle\langle\Gamma_\kappa(\mathbf{r}'_t)\rangle\langle G(\mathbf{r}_t|\mathbf{r}_0,f)G(\mathbf{r}|\mathbf{r}_t,f)G^*(\mathbf{r}'_t|\mathbf{r}_0,f)G^*(\mathbf{r}|\mathbf{r}'_t,f)\rangle\\
&\quad + \langle\Gamma_d(\mathbf{r}_t)\rangle\langle\Gamma_d(\mathbf{r}'_t)\rangle\langle\nabla G(\mathbf{r}_t|\mathbf{r}_0,f)\cdot\nabla G(\mathbf{r}|\mathbf{r}_t,f)\times\nabla G^*(\mathbf{r}'_t|\mathbf{r}_0,f)\cdot\nabla G^*(\mathbf{r}|\mathbf{r}'_t,f)\rangle\\
&\quad + k^2\langle\Gamma_\kappa(\mathbf{r}_t)\rangle\langle\Gamma_d(\mathbf{r}'_t)\rangle\langle G(\mathbf{r}_t|\mathbf{r}_0,f)G(\mathbf{r}|\mathbf{r}_t,f)\nabla G^*(\mathbf{r}'_t|\mathbf{r}_0,f)\cdot\nabla G^*(\mathbf{r}|\mathbf{r}'_t,f)\rangle\\
&\quad + k^2\langle\Gamma_\kappa(\mathbf{r}'_t)\rangle\langle\Gamma_d(\mathbf{r}_t)\rangle\langle G^*(\mathbf{r}'_t|\mathbf{r}_0,f)G^*(\mathbf{r}|\mathbf{r}'_t,f)\nabla G(\mathbf{r}_t|\mathbf{r}_0,f)\cdot\nabla G(\mathbf{r}|\mathbf{r}_t,f)\rangle]\,dV_t\,dV'_t\\
&- (4\pi)^2 \iiint_{V_S}\iiint_{V_S} [k^4\langle\Gamma_\kappa(\mathbf{r}_t)\rangle\langle\Gamma_\kappa(\mathbf{r}'_t)\rangle\langle G(\mathbf{r}_t|\mathbf{r}_0,f)G(\mathbf{r}|\mathbf{r}_t,f)\rangle\langle G^*(\mathbf{r}'_t|\mathbf{r}_0,f)G^*(\mathbf{r}|\mathbf{r}'_t,f)\rangle\\
&\quad + \langle\Gamma_d(\mathbf{r}_t)\rangle\langle\Gamma_d(\mathbf{r}'_t)\rangle\langle\nabla G(\mathbf{r}_t|\mathbf{r}_0,f)\cdot\nabla G(\mathbf{r}|\mathbf{r}_t,f)\rangle\langle\nabla G^*(\mathbf{r}'_t|\mathbf{r}_0,f)\cdot\nabla G^*(\mathbf{r}|\mathbf{r}'_t,f)\rangle\\
&\quad + k^2\langle\Gamma_\kappa(\mathbf{r}_t)\rangle\langle\Gamma_d(\mathbf{r}'_t)\rangle\langle G(\mathbf{r}_t|\mathbf{r}_0,f)G(\mathbf{r}|\mathbf{r}_t,f)\rangle\langle\nabla G^*(\mathbf{r}'_t|\mathbf{r}_0,f)\cdot\nabla G^*(\mathbf{r}|\mathbf{r}'_t,f)\rangle\\
&\quad + k^2\langle\Gamma_\kappa(\mathbf{r}'_t)\rangle\langle\Gamma_d(\mathbf{r}_t)\rangle\langle G^*(\mathbf{r}'_t|\mathbf{r}_0,f)G^*(\mathbf{r}|\mathbf{r}'_t,f)\rangle\langle\nabla G(\mathbf{r}_t|\mathbf{r}_0,f)\cdot\nabla G(\mathbf{r}|\mathbf{r}_t,f)\rangle]\,dV_t\,dV'_t.\\
&= \mathrm{Term}^{\mathrm{TH}}_{(\mathrm{Var}(\Gamma_\kappa),\mathrm{Var}(\Gamma_d),\mathrm{Covar}(\Gamma_\kappa,\Gamma_d))} + \mathrm{Term}^{\mathrm{TH}}_{(<\Gamma_\kappa>,<\Gamma_d>)} && \text{(A.18b)}
\end{aligned}$$

In Section A.2, we show, using Monte Carlo simulations in a standard Pekeris waveguide, that the matched filtered scattered intensity derived in Equation (A.17c) can be approximated by the first term of the total time harmonic variance, also given by Galinde *et al.*, [27] as:

$$\mathrm{Var}(\Phi_S(\mathbf{r}_S|\mathbf{r},\mathbf{r}_0,f)) = \mathrm{Monopole}_{TH} + \mathrm{Dipole}_{TH} + \mathrm{Cross}_{TH}, \qquad \text{(A.18c)}$$

where,

$$\begin{aligned}
\mathrm{Monopole}_{TH} &= (4\pi)^2 \iiint_{V_S} V_c(\mathbf{r}_S,z_t)k^4\mathrm{Var}(\Gamma_\kappa)\langle|G(\mathbf{r}_t|\mathbf{r}_0,f_c)|^2|G(\mathbf{r}|\mathbf{r}_t,f_c)|^2\rangle dV_t,\\
\mathrm{Dipole}_{TH} &= (4\pi)^2 \iiint_{V_S} V_c(\mathbf{r}_S,z_t)\mathrm{Var}(\Gamma_d)\langle|\nabla G(\mathbf{r}_t|\mathbf{r}_0,f_c)\cdot\nabla G(\mathbf{r}|\mathbf{r}_t,f_c)|^2\rangle dV_t,\\
\mathrm{Cross}_{TH} &= (4\pi)^2 \iiint_{V_S} V_c(\mathbf{r}_S,z_t)k^2\mathrm{Covar}(\Gamma_\kappa,\Gamma_d)\\
&\qquad \langle 2\Re\{G(\mathbf{r}_t|\mathbf{r}_0,f)G(\mathbf{r}|\mathbf{r}_t,f_c)\nabla G^*(\mathbf{r}_t|\mathbf{r}_0,f_c)\cdot\nabla G^*(\mathbf{r}|\mathbf{r}_t,f_c)\}\rangle]\,dV_t \qquad \text{(A.18d)}
\end{aligned}$$